A&A 571, A8 (2014)
DOI: 10.1051/0004-6361/201321538

Astronomy & Astrophysics
Special feature

Planck 2013 results

Planck 2013 results. VIII. HFI photometric calibration and mapmaking

Planck Collaboration: P. A. R. Ade[84], N. Aghanim[58], C. Armitage-Caplan[89], M. Arnaud[71], M. Ashdown[67,6], F. Atrio-Barandela[18], J. Aumont[58], C. Baccigalupi[83], A. J. Banday[92,10], R. B. Barreiro[64], E. Battaner[93], K. Benabed[59,91], A. Benoît[56], A. Benoit-Lévy[24,59,91], J.-P. Bernard[92,10], M. Bersanelli[34,49], B. Bertincourt[58], P. Bielewicz[92,10,83], J. Bobin[71], J. J. Bock[65,11], J. R. Bond[9], J. Borrill[14,86], F. R. Bouchet[59,91], F. Boulanger[58], M. Bridges[67,6,62], M. Bucher[1], C. Burigana[48,32], J.-F. Cardoso[72,1,59], A. Catalano[73,69], A. Challinor[62,67,12], A. Chamballu[71,15,58], R.-R. Chary[55], X. Chen[55], H. C. Chiang[27,7], L.-Y Chiang[61], P. R. Christensen[79,37], S. Church[88], D. L. Clements[54], S. Colombi[59,91], L. P. L. Colombo[23,65], C. Combet[73], F. Couchot[68], A. Coulais[69], B. P. Crill[65,80], A. Curto[6,64], F. Cuttaia[48], L. Danese[83], R. D. Davies[66], P. de Bernardis[33], A. de Rosa[48], G. de Zotti[44,83], J. Delabrouille[1], J.-M. Delouis[59,91], F.-X. Désert[52], C. Dickinson[66], J. M. Diego[64], H. Dole[58,57], S. Donzelli[49], O. Doré[65,11], M. Douspis[58], X. Dupac[39], G. Efstathiou[62], T. A. Enßlin[76], H. K. Eriksen[63], C. Filliard[68], F. Finelli[48,50], O. Forni[92,10], M. Frailis[46], E. Franceschi[48], S. Galeotta[46], K. Ganga[1], M. Giard[92,10], G. Giardino[40], Y. Giraud-Héraud[1], J. González-Nuevo[64,83], K. M. Górski[65,94], S. Gratton[67,62], A. Gregorio[35,46], A. Gruppuso[48], F. K. Hansen[63], D. Hanson[77,65,9], D. Harrison[62,67], G. Helou[11], S. Henrot-Versillé[68], C. Hernández-Monteagudo[13,76], D. Herranz[64], S. R. Hildebrandt[11], E. Hivon[59,91], M. Hobson[6], W. A. Holmes[65], A. Hornstrup[16], W. Hovest[76], K. M. Huffenberger[25], A. H. Jaffe[54], T. R. Jaffe[92,10], W. C. Jones[27], M. Juvela[26], E. Keihänen[26], R. Keskitalo[21,14], T. S. Kisner[75], R. Kneissl[38,8], J. Knoche[76], L. Knox[28], M. Kunz[17,58,3], H. Kurki-Suonio[26,42], G. Lagache[58], J.-M. Lamarre[69], A. Lasenby[6,67], R. J. Laureijs[40], C. R. Lawrence[65], M. Le Jeune[1], E. Lellouch[70], R. Leonardi[39], C. Leroy[58,92,10], J. Lesgourgues[90,82], M. Liguori[31], P. B. Lilje[63], M. Linden-Vørnle[16], M. López-Caniego[64], P. M. Lubin[29], J. F. Macías-Pérez[73], B. Maffei[66], N. Mandolesi[48,5,32], M. Maris[46], D. J. Marshall[71], P. G. Martin[9], E. Martínez-González[64], S. Masi[33], M. Massardi[47], S. Matarrese[31], F. Matthai[76], L. Maurin[1], P. Mazzotta[36], P. McGehee[55], P. R. Meinhold[29], A. Melchiorri[33,51], L. Mendes[39], A. Mennella[34,49], M. Migliaccio[62,67], S. Mitra[53,65], M.-A. Miville-Deschênes[58,9], A. Moneti[59], L. Montier[92,10], R. Moreno[70], G. Morgante[48], D. Mortlock[54], D. Munshi[84], J. A. Murphy[78], P. Naselsky[79,37], F. Nati[33], P. Natoli[32,4,48], C. B. Netterfield[19], H. U. Nørgaard-Nielsen[16], F. Noviello[66], D. Novikov[54], I. Novikov[79], S. Osborne[88], C. A. Oxborrow[16], F. Paci[83], L. Pagano[33,51], F. Pajot[58], R. Paladini[55], D. Paoletti[48,50], B. Partridge[41], F. Pasian[46], G. Patanchon[1], T. J. Pearson[11,55], O. Perdereau[68,⋆], L. Perotto[73], F. Perrotta[83], F. Piacentini[33], M. Piat[1], E. Pierpaoli[23], D. Pietrobon[65], S. Plaszczynski[68], E. Pointecouteau[92,10], G. Polenta[4,45], N. Ponthieu[58,52], L. Popa[60], T. Poutanen[42,26,2], G. W. Pratt[71], G. Prézeau[11,65], S. Prunet[59,91], J.-L. Puget[58], J. P. Rachen[20,76], M. Reinecke[76], M. Remazeilles[66,58,1], C. Renault[73], S. Ricciardi[48], T. Riller[76], I. Ristorcelli[92,10], G. Rocha[65,11], C. Rosset[1], G. Roudier[1,69,65], B. Rusholme[55], D. Santos[73], G. Savini[81], D. Scott[22], E. P. S. Shellard[12], L. D. Spencer[84], J.-L. Starck[71], V. Stolyarov[6,67,87], R. Stompor[1], R. Sudiwala[84], R. Sunyaev[76,85], F. Sureau[71], D. Sutton[62,67], A.-S. Suur-Uski[26,42], J.-F. Sygnet[59], J. A. Tauber[40], D. Tavagnacco[46,35], S. Techene[59], L. Terenzi[48], M. Tomasi[49], M. Tristram[68], M. Tucci[17,68], G. Umana[43], L. Valenziano[48], J. Valiviita[42,26,63], B. Van Tent[74], P. Vielva[64], F. Villa[48], N. Vittorio[36], L. A. Wade[65], B. D. Wandelt[59,91,30], D. Yvon[15], A. Zacchei[46], and A. Zonca[29]

(Affiliations can be found after the references)

Received 21 March 2013 / Accepted 8 March 2014

ABSTRACT

This paper describes the methods used to produce photometrically calibrated maps from the *Planck* High Frequency Instrument (HFI) cleaned, time-ordered information. HFI observes the sky over a broad range of frequencies, from 100 to 857 GHz. To obtain the best calibration accuracy over such a large range, two different photometric calibration schemes have to be used. The 545 and 857 GHz data are calibrated by comparing flux-density measurements of Uranus and Neptune with models of their atmospheric emission. The lower frequencies (below 353 GHz) are calibrated using the solar dipole. A component of this anisotropy is time-variable, owing to the orbital motion of the satellite in the solar system. Photometric calibration is thus tightly linked to mapmaking, which also addresses low-frequency noise removal. By comparing observations taken more than one year apart in the same configuration, we have identified apparent gain variations with time. These variations are induced by non-linearities in the read-out electronics chain. We have developed an effective correction to limit their effect on calibration. We present several methods to estimate the precision of the photometric calibration. We distinguish relative uncertainties (between detectors, or between frequencies) and absolute uncertainties. Absolute uncertainties lie in the range from 0.54% to 10% from 100 to 857 GHz. We describe the pipeline used to produce the maps from the HFI timelines, based on the photometric calibration parameters, and the scheme used to set the zero level of the maps a posteriori. We also discuss the cross-calibration between HFI and the SPIRE instrument on board *Herschel*. Finally we summarize the basic characteristics of the set of HFI maps included in the 2013 *Planck* data release.

Key words. cosmic background radiation – cosmology: observations – surveys – methods: data analysis

⋆ Corresponding authors: O. Perdereau, e-mail: perdereau@lal.in2p3.fr; G. Lagache, e-mail: guilaine.lagache@ias.u-psud.fr

Table 1. Parameters of the solar dipole, as measured by WMAP (Hinshaw et al. 2009).

Amplitude [mK_{CMB}]	3.355 ± 0.008
Galactic longitude [°]	263.99 ± 0.14
Galactic latitude [°]	41.74 ± 0.03

1. Introduction

This paper, one of a set associated with the 2013 release of data from the *Planck* mission[1], describes the processing applied to *Planck* High Frequency Instrument (HFI) cleaned time-ordered information (TOI) to produce photometrically-calibrated sky maps.

Cosmic microwave background (CMB) experiments can be calibrated using the dipole anisotropy induced by the motion of the instrument relative to the cosmological frame. This anisotropy is naturally separated into two components: we refer to the component generated by the motion of Planck around the sun as the *orbital dipole*, and that generated by the sun's motion relative to the CMB as the *solar dipole*.

In principle, the orbital dipole is the most precise calibrator, as it depends on the very well known orbital parameters and the temperature of the CMB, measured precisely by the COBE-FIRAS experiment (Mather et al. 1999). However, calibration using the orbital dipole involves comparison of data taken at large time separation (typically 6 months), and the precision one can achieve using this calibrator is thus directly linked to that of the time stability of the data, and to the precision reached in addressing any time variable systematics. We have identified one such systematic, induced by non-linearities in the analogue-to-digital converters of the bolometers' read-out electronic chain, and for the present release have chosen to use the solar dipole, based on the measurement of the solar dipole parameters from WMAP (Hinshaw et al. 2009), as the main calibrator for the 100 to 353 GHz channels. These parameters are summarized in Table 1.

At high frequency ($\nu \geq 500$ GHz), the dipole becomes too faint with respect to the Galactic foregrounds to give an accurate calibration. Although we used the Galactic emission as measured by FIRAS for the calibration of the *Planck* early papers (Planck HFI Core Team 2011a), we have now obtained a better accuracy using planet measurements. Thus, the absolute calibration of the two high-frequency channels is done using Uranus and Neptune.

At all frequencies, the zero levels of the maps are obtained by assuming no Galactic emission at zero gas column density, and adding the cosmic infrared background (CIB) mean level.

The paper is organized as follows. We first summarize the mapmaking procedure (Sect. 2). We outline the calibration method used for the CMB-dominated channels (100 to 353 GHz) in Sect. 3. We discuss in this section unexpected response variations with time, and present an effective correction. We then detail the calibration for the 545 and 857 GHz channels (Sect. 4) and describe how the zero level of the maps can be fixed (Sect. 5). We finally quantify the accuracy of the photometric calibration, and give basic characteristics of the delivered maps in Sect. 6. Conclusion are given in Sect. 7.

2. Pipeline for map production

The products of the HFI mapmaking pipeline are maps of I, Q and U, together with their covariances, pixelized according to the `HEALPix` scheme (Górski et al. 2005) with a resolution parameter $N_{\rm side} = 2048$. For a given channel, data sample i may be described as

$$d_i = G\left(I_p + \frac{1-\eta}{1+\eta}\left(Q_p \cos 2\psi_i + U_p \sin 2\psi_i\right)\right) + n_i, \quad (1)$$

where p denotes the sky pixel with Stokes parameters I_p, Q_p and U_p, n_i is the noise realization, η is the cross-polarization parameter (equal to 1 for an ideal spider-web bolometer and 0 for an ideal polarization sensitive bolometer), ψ_i is the detector orientation on the sky, at sample i, and G is the detector's gain. Given *Planck*'s scanning strategy, reconstructing I, Q and U requires combining measurements from several detectors for most pixels. According to bolometer models, and given the stability of the HFI operational conditions during the mission, G is not expected to vary significantly,

In order to deal efficiently with the large HFI data set and the large number of maps to be produced, we use a two-step scheme to make maps from the HFI TOIs. The first step takes advantage of the redundancy of the observations on the sky. For each detector, we average the measurements in each `HEALPix` pixel visited during a stable pointing period (hereafter called *ring*), into an intermediate product, called an HPR for `HEALPix` Pixels Ring. Subsequent calibration and mapmaking operations use the HPR as input. As we produce `HEALPix` maps with the resolution parameter $N_{\rm side}$ set to 2048 we use the same internal resolution for building the HPR.

The in-flight noise of the HFI detectors, after TOI processing, is mostly white at high frequency, with a "$1/f$" increase at low frequency (Planck HFI Core Team 2011a). In such a case, a destriping approach is well suited for the mapmaking (Ashdown et al. 2009). In this approach, the noise in a ring r is represented by an offset, denoted by $\boldsymbol{o}_r$, and a white noise part $\boldsymbol{n}$, which is uncorrelated with the low-frequency noise. We may then reformulate Eq. (1) as

$$\boldsymbol{d}_i = G \times \mathsf{A}_{ip} \cdot \mathsf{T}_p + \Gamma_{ir} \cdot \boldsymbol{o}_r + \boldsymbol{n}_i, \quad (2)$$

where T represents the sky (which may be a 3-vector if polarization is accounted for) in pixel p, A is the pointing matrix (which makes the link between data samples and their positions on the sky) and Γ is the matrix folding the ring onto samples. From the above equation, $\boldsymbol{o}_r$ are derived through maximum likelihood. As there is a degeneracy between the average of the offsets and the zero level of the maps, we impose the constraint $\langle \boldsymbol{o} \rangle = 0$. Tristram et al. (2011) have shown that with scanning and noise like those of HFI, an accurate reconstruction of the offsets $\boldsymbol{o}_r$ requires a precise measurement of G for each channel.

In addition, some signal components vary with time, adding more complexity to Eq. (2). Such components include the zodiacal light emission, the CMB dipole anisotropy component induced by the motion of the satellite with respect to the solar System, and the far sidelobe (FSL) pick-up signal. Time variability of the former comes from the variation of the observation angle of the solar System region emitting this radiation, due to the ellipticity and cycloid modulation of the satellite's orbit.

[1] *Planck* (`http://www.esa.int/Planck`) is a project of the European Space Agency (ESA) with instruments provided by two scientific consortia funded by ESA member states (in particular the lead countries France and Italy), with contributions from NASA (USA) and telescope reflectors provided by a collaboration between ESA and a scientific consortium led and funded by Denmark.

The FSL are discussed in Planck Collaboration VII (2014) and Planck Collaboration XIV (2014). Accounting for these components in the mapmaking process requires an accurate calibration. Moreover, we need to take into account the low-frequency noise in the calibration process, so both operations (mapmaking and calibration) are interleaved.

For the production of the maps of the 2013 HFI data release, we followed a four-step process.

1. We first build the HPR for all detectors, for three data sets: all the data for each ring, and (for null tests) the data from just the first or just the second half of each ring.
2. We then apply the following calibration operations to the HPR:
   - solar dipole calibration, which sets the overall calibration factors for the 100–353 GHz detectors,
   - planet calibration (Uranus and Neptune), which is used to get the calibration factors for the 545–857 GHz detectors,
   - determine the relative gain variations over time of the 100−217 GHz detectors, using the `bogopix` tool (see Sect. 3.3).
3. For each data set we then do the destriping and projections, using the `polkapix` tool that was thoroughly validated in Tristram et al. (2011). We compute one set of offsets using the full mission (29 months) data set, and then use these offsets to compute the maps for the full mission, as well as for restricted time intervals (corresponding to each individual survey, and to the 15-months nominal mission). Maps are built by simple co-addition in each pixel of the destriped, calibrated, and time varying component-subtracted signal. We subtract the WMAP measured CMB dipole from all our maps, using the non-relativistic approximation.
4. The zero-levels for the maps are set a posteriori.

We have produced single-detector temperature maps, as well as temperature and polarization maps using all the detectors of a single frequency and some detector subsets. We have also produced hit-count maps and variance maps for the I, Q and U values computed in each pixel. Overall, a total of about 6500 sky maps have been produced. We used this data set to evaluate the performance of the photometric calibration. Note that the HFI pipeline we have described is quite similar to that used for the Low Frequency Instrument (LFI; Planck Collaboration II 2014).

In order to take into account the Galactic signal integrated in the FSL and zodiacal light (hereafter called `zodi`) components, which vary in time, we have constructed templates for the combination of both components at frequencies where Galactic emission in the FSL matters, i.e., 545 and 857 GHz, and of `zodi` only at lower frequencies, as described in Planck Collaboration XIV (2014). These templates are used to build HPRs. We provide two sets of maps. The first set is built without removing these spurious components, while the second set is the differences between maps from the previous set and maps from which the `zodi` and FSL have been removed. The difference maps might be can be used to correct the HFI maps for specific applications.

In the following sections we will describe the calibration procedures and then assess their performance, and present some characteristics of the resulting maps.

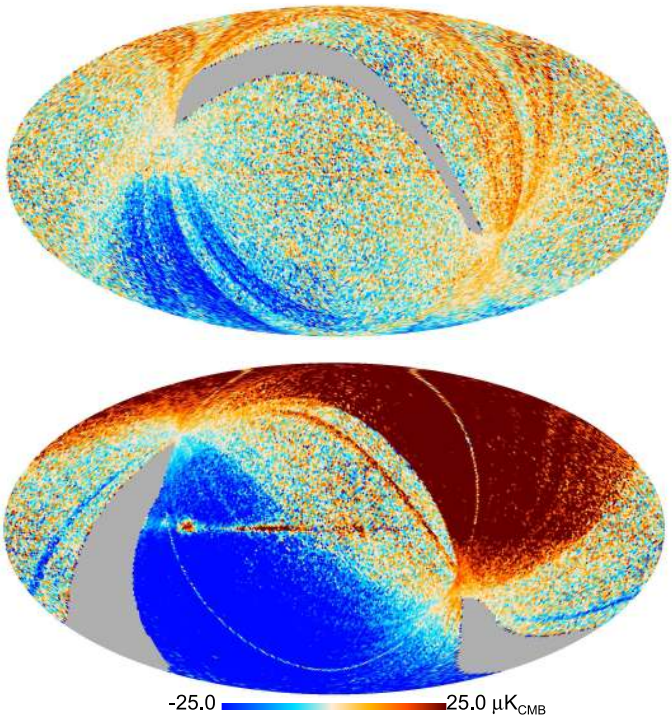

Fig. 1. Differences between temperature maps built using data from detector 143-1a, for Surveys 1 and 3 (*top*) and 2 and 4 (*bottom*). In both cases, large-scale features appear. Their amplitude and disposition on the sky are compatible with residuals from the solar dipole, due to time variations of the detector gain, of the order of 1 to 2%. These residuals should be compared to the amplitudes of the solar dipole, 3.353 mK$_{CMB}$, and to the orbital dipole that is about 10 times lower.

3. Photometric calibration of the low-frequency channels: dipole-based calibration

3.1. ADC non-linearities and calibration

With a larger data set than that analyzed in Planck HFI Core Team (2011b), we could ideally use an orbital-dipole-based calibration, as described in Tristram et al. (2011). However, the additional redundancies revealed new systematic effects, ADC non-linearities and very long time constants (of the order of a few seconds) with very low energy content in the system's response. The former induce apparent gain variations with time. The latter shifts the CMB dipole a few arcmin in the scan direction, and hence creates leaks from the solar dipole into the orbital dipole signal. These systematic effects prevented us from using the orbital dipole calibration. The very long time constants were identified after correcting for the ADC non-linearities, and have not yet been fully characterized yet. Both corrections will be implemented in the *Planck* 2014 data release.

Effects of such ADC-induced gain variations are clearly visible when comparing Survey 3 with Survey 1 or Survey 2 with Survey 4. As an example, in Fig. 1 we show survey difference maps for one 143 GHz detector, built using the calibration and mapmaking scheme presented in Planck HFI Core Team (2011b). Large-scale dipolar features, aligned with the solar dipole, are prominent in these maps. This shows that the constant gain assumption used to build these maps is incorrect.

Intrinsic bolometer sensitivity variations cannot explain such gain variations. The HFI bolometers have been precisely characterized in flight using a dedicated sequence of $V(I)$

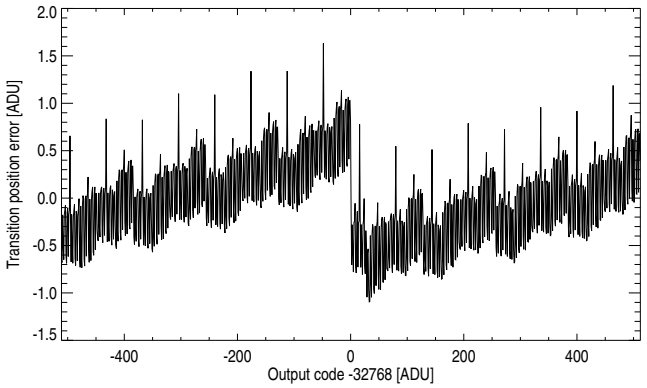

Fig. 2. Error on transition code positions measured on one chip around the ADC mid-scale, on the ground on a spare ADC. The largest error occurs at the sign transition, but errors of about 1 ADU also occur regularly every 64 steps.

measurements, during the post-launch verification phase and end-of-life periods. The static bolometer models predict that changes of their background during the observations could not explain response variations larger than 0.1%. In addition, such variations are corrected for within the HFI DPC pipeline. In our present understanding, these apparent response variations are the result of imperfections in the linearity of the analogue-to-digital converters (ADC) used in the bolometer read-out units. The variation of the bolometer background with time and the unevenness in the ADC quantization steps leads, at first order, to an apparent gain variation in the electronic chain. These non-linearities may also affect signals differently depending on their amplitude, for example the solar and orbital dipoles.

Figure 2 shows the errors on the transition code positions measured on a spare ADC chip around the mid-scale, which is the most populated area. These "integrated non-linearities" (INL) present a prominent feature in all channels: the central step is always too narrow. In addition to this, the 64-code, nearly periodic patterns contribute to the apparent gain variations, making it difficult to predict the consequence of such errors on the reconstructed, demodulated bolometer signal. Such an INL effect has however been included in full mission simulations, and it reproduces qualitatively the gain variation features observed in real flight data, with an amplitude of about ±1%. This is larger than the required calibration precision of the 100 to 217 GHz channels.

In order to precisely correct all the data for this effect, we need accurate measurements of all the ADC INLs, together with a good model for the bolometer raw signal (including systematics). Mapping the ADC response required more data than were acquired before the end of the HFI cold lifetime, so a dedicated campaign has been conducted over several months, at a focal plane temperature of about 4 K, to obtain a clean ADC characterization on Gaussian noise. Correcting this effect needs to be carried out prior to the TOI processing steps, and will require thorough checks of any products. At the time of writing, correction procedures are being intensively tested but they have not been included in the 2013 *Planck* data release.

In the absence of a full correction procedure, we had to develop an effective method to address the apparent bolometer gain variations that arise from the ADC non-linearities. In this method, the absolute scale is fixed by the solar dipole, to ensure a better robustness against higher-order non-linearities, as described in Sect. 3.2. Relative gains are determined using the scanning redundancies, as explained in Sect. 3.3.

3.2. Solar dipole calibration

The photometric calibration of the 100–353 GHz bolometers is based on the CMB dipole.

We estimate one value of the detector gain for each ring through a template fit of the HPR data. We fit the coefficients of a linear combination of dipole, Galactic signal, and noise, neglecting the CMB and the polarization:

$$\boldsymbol{d} = g_r^{\mathrm{D}}.\boldsymbol{t}_{\mathrm{D}} + g_r^{\mathrm{G}}.\boldsymbol{t}_{\mathrm{G}} + c_r + \boldsymbol{n}. \quad (3)$$

Here $\boldsymbol{d}$ represents the HPR samples from ring r, $\boldsymbol{t}_{\mathrm{D}}$ is the value of the total (solar and orbital) kinematic dipole, $\boldsymbol{t}_{\mathrm{G}}$ is a model for the Galactic emission, and $\boldsymbol{n}$ is the white component of the noise. For simplicity, we used a non-relativistic approximation, as explained in Appendix A.2. We do not take into account the smearing of the dipole by the instrumental beam in our procedure, as justified in Appendix A.3. We simultaneously fit three parameters: g_r^{D}, the gain of the kinematic dipole; g_r^{G}, the gain of the Galactic model; and c_r, a constant accounting for the low-frequency noise.

As the satellite scans circles on the sky, the ratio of the dipole and Galactic signal amplitudes varies. We use a Galactic model to obtain a measurement of the dipole gain, even in rings where the dipole amplitude is low. However, imperfection of that model may lead to bias in the dipole gain. To reduce this bias, we exclude pixels with a Galactic latitude lower than 9°. Because we calibrate on the kinematic dipole, we do not use the gain g_r^{G} in what follows. Pixels contaminated by point sources listed in the *Planck* Catalogue of Compact Sources (Planck Collaboration XXVIII 2014) are also excluded. The best model we have for the sky emission at the HFI frequencies being HFI measurements themselves, we use HFI sky maps at the detector frequency as a Galactic model, as shown in Appendix B.

Results of the gain estimation for each ring are shown in Fig. 3 for one detector (143-1a) . We can see that the gain estimate is less accurate on some ring intervals. This is due to the *Planck* scanning strategy: these intervals correspond to epochs when the *Planck* spin axis is orthogonal to the dipole direction. We can also see the apparent ring-by-ring gain variations, of the order of ±1%, explained in Sect. 3.1. To show this more clearly, the figure compares the ring-by-ring variations reconstructed in Surveys 1 and 2 with those from Surveys 3 and 4.

The final gain value for each detector, hereafter denoted by $\tilde{G}^{\mathrm{SD}}$, is defined as the average of these estimates between rings 2000 and 6000, between which the individual measurements for each ring have a dispersion of less than 1%.

3.3. Effective correction and characterization

In order to handle time variation of the bolometer gains, we set up an effective correction tool, called `bogopix` (Perdereau 2006). We start from Eq. (2), but take explicitly into account the orbital dipole $\boldsymbol{t}_{\mathrm{Do}}$, which is time-variable, and also fit the gains $\boldsymbol{g}_r$ for each bolometer independently. The problem finally reads

$$\boldsymbol{d} = \boldsymbol{g}_r(\mathsf{A} \cdot \mathsf{T} + \boldsymbol{t}_{\mathrm{Do}}) + \Gamma \cdot \boldsymbol{o}_r + \boldsymbol{n}, \quad (4)$$

where r is the ring number. The unknowns are the offsets $\boldsymbol{o}_r$, the sky signal represented by T, and the gains $\boldsymbol{g}_r$, sampled using one

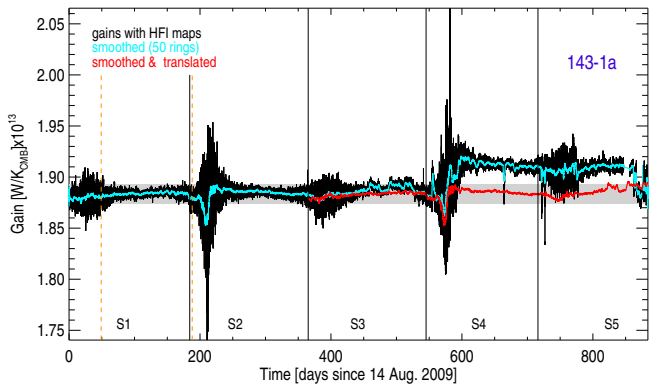

Fig. 3. Solar dipole gain reconstructed ring-by-ring for one HFI bolometer. The thin black line represent the raw values, and the thick cyan line is a smoothed rendition with a width of 50 rings (about 2 days). We have indicated the conventional boundaries of the surveys as black vertical lines. The orange vertical dashed lines indicate the interval in which we compute the gain $\tilde{G}^{\rm SD}$ (computed between rings 2000 and 6000, or approximately days 60 and 190). The red curve shows the smoothed gain variation shifted to match the repetition in Surveys 3 and 4 of the scan strategy followed in Surveys 1 and 2 (note that the scan strategy for Survey 5 differs from that of Survey 3). The grey band highlights a ±0.5% excursion around the averaged gain $\tilde{G}^{\rm SD}$. The observed ∼1% variations explain the large-scale residuals seen in Fig. 1.

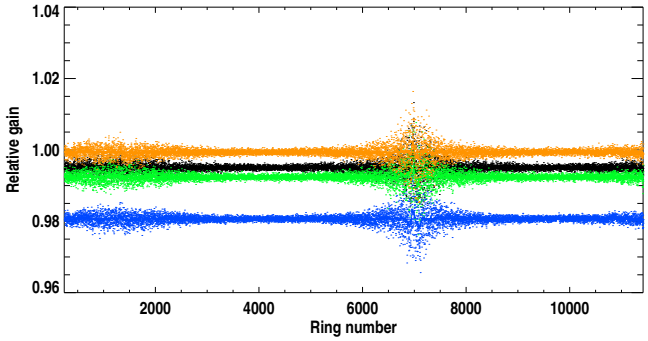

Fig. 4. Example of results obtained with `bogopix` on the simulated data set used in Tristram et al. (2011), where constant gains biases were applied. The colours distinguish four different bolometers. Dots correspond to individual measurements, and the thick line is a smoothed representation of these results with a 50 ring width. We plot relative reconstructed gains, with respect to their unbiased value. In this simulation, each bolometer's data was biased by factors of respectively 1.98 (blue), 0.77 (green), 0.50 (black) and 0.07% (orange) respectively which is precisely reflected by the recovered `bogopix` value.

value per ring. Since the orbital dipole is an absolute calibrator, the solution for $\boldsymbol{g}_r$ should also fix the absolute photometric calibration.

We take advantage of the low amplitude of the observed gain variations to linearize this nonlinear problem, following an iterative approach. Starting from an approximate solution for the gains $\boldsymbol{g}_r$ and sky maps T, we determine the variations with respect to these, $\boldsymbol{\delta g}_r$ and $\delta\mathsf{T}$, by solving :

$$\boldsymbol{d} = (\boldsymbol{g}_r + \boldsymbol{\delta g}_r)(\mathsf{A}\cdot(\mathsf{T}+\delta\mathsf{T}) + \boldsymbol{t}_{\rm Do}) + \Gamma\cdot\boldsymbol{o}_r + \boldsymbol{n} \quad (5)$$

$$\approx \boldsymbol{g}_r(\mathsf{A}\cdot(\mathsf{T}+\delta\mathsf{T}) + \boldsymbol{t}_{\rm Do}) + \boldsymbol{\delta g}_r(\mathsf{A}\cdot\mathsf{T} + \boldsymbol{t}_{\rm Do}) + \Gamma\cdot\boldsymbol{o}_r + \boldsymbol{n}. \quad (6)$$

The linearized Eq. (6) may then be solved for $\boldsymbol{\delta g}_r$, $\delta\mathsf{T}$ and $\boldsymbol{o}_r$ by a conjugate-gradient method. Using $\boldsymbol{\delta g}_r$ and $\delta\mathsf{T}$, the gains $\boldsymbol{g}_r$ and sky maps T can be updated. This process is iterated until a satisfactory solution is reached. To initialize the iterations, we start from the constant gain solution. We stop when the relative change in the χ^2 derived from Eq. (4) is low enough (in practice, when the change is less than 10^{-6}). This approach is similar to the one used for the LFI calibration (Planck Collaboration V 2014). It was successfully tested using the data set of Tristram et al. (2011), derived from simulated timelines with a *Planck*-like scanning strategy, realistic noise (both for the white and $1/f$ components), Gaussian beams, and delta-function bandpasses, for four 143 GHz polarization-sensitive bolometers over about 12 000 rings. Figure 4 presents gains reconstructed with `bogopix` on simulated data, and compares them with the constant input gain values. From these results, we see that the precision of the gain value reconstructed for a single ring is about 0.5% (which is comparable with the global precision of 5×10^{-5} for a constant gain for 12 000 rings found in Tristram et al. 2011). We computed the gain variations using single-detector data, thus neglecting polarization. As in destriping (Tristram et al. 2011), gradients within the sky pixels used for T will limit the accuracy of the gain determination. These gradients increase with frequency. Moreover, the ADC non-linearity will induce biases in the signal used for the gain determination. As this signal's dynamic range increases with frequency, we expect this bias also to increase with frequency. For these reasons, we used `bogopix` to determine an effective correction for the apparent gain variations only for frequencies ≤217 GHz. To avoid the central part of the Galactic plane and point sources, we used the mask used for destriping in the *Planck* Early Results paper (Planck HFI Core Team 2011b, Fig. 32).

As shown in Fig. 5, the variations of the gains g_r found with `bogopix` follow nicely those from the solar dipole calibration ($g_r^{\rm D}$) in the regions where this signal is large. The lower level of fast variations from `bogopix` in the time intervals where the scan lies close to the solar dipole equator and at the same time close to the Galactic plane, indicates that the `bogopix` results are less biased for these rings. We observe apparent gain variations on time scales of a few hour as well as months, with amplitudes of 1 to 2% maximum, largely uncorrelated from one detector to another.

The averaged gain level determined by the two methods are, however, different by 0.5 to 1%, and the difference varies from one detector to another. We believe this is due to the different scales of the calibrating signals in the two methods: the absolute scale of `bogopix` results is set by that of the orbital dipole, a factor of 5 to 10 lower in amplitude that the solar dipole used in the other method. These signals are thus affected to different degrees by the ADC non-linearities. In the simplest case, the effect of the non-uniformity of the ADC digitization steps is a fixed offset (positive or negative) added on top of the signal, when this signal oversteps a given level, so the resulting calibration bias will be lower for the largest calibration signal.

We study the difference between the averaged solar dipole gain, $\tilde{G}^{\rm SD}$, and the average of the `bogopix` results, g_r, in the same ring interval, denoted by $\tilde{G}^{\rm bog}$. We introduce another calibration process, based on the orbital dipole as described in Tristram et al. (2011), together with `bogopix` gains, renormalized so that they average to 1 between rings 2000 and 6000 (corresponding to days 60 and 190 approximately), to correct for the apparent relative gain variations. This produces another estimate of the absolute gain, $G^{\rm OD}$. The relative differences, $(\tilde{G}^{\rm SD} - G^{\rm OD})/\tilde{G}^{\rm SD}$, are shown in Fig. 6 for each 143 GHz detector. Both methods agree with each other within 0.05 to 0.1%. We conclude that the difference between $\tilde{G}^{\rm SD}$ and $\tilde{G}^{\rm bog}$ is genuine

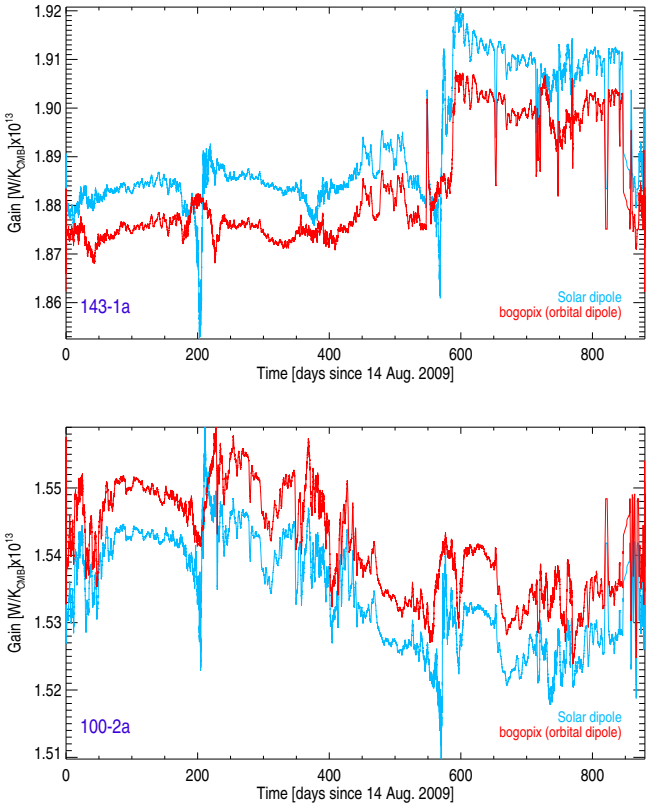

Fig. 5. `bogopix` results for two HFI detectors, compared with those from the solar dipole calibration. Gain values for individual rings have been smoothed with a width of 50 rings (about 2 days), to increase the signal-to-noise ratio. There is good agreement of the relative gain variations between the `bogopix` results and those obtained from the HFI maps, except for the time intervals where the solar dipole amplitude is lower than the Galactic emission. The averaged value of the gains are, however, offset by factors (different from one detector to the other) of the order of 0.5 to 1%.

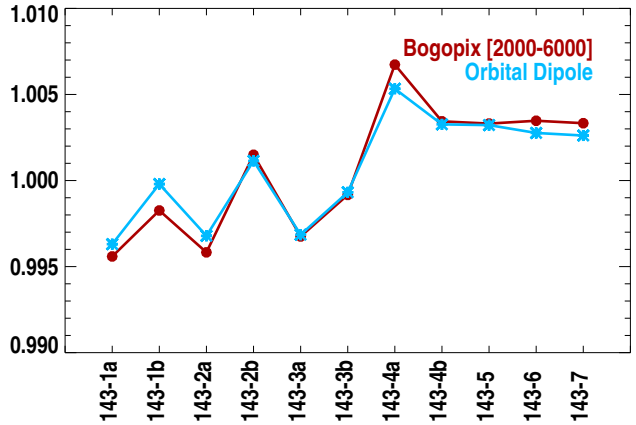

Fig. 6. Relative differences of the orbital dipole calibration ($G^{\rm OD}$, blue) and the average of `bogopix` gains ($\tilde{G}^{\rm bog}$, red), with respect to the solar dipole calibration results($\tilde{G}^{\rm SD}$), for the 143 GHz HFI detectors. Both schemes produce gains within 0.1% of each other, which shows that they are both affected by the same systematics (the ADC non-linearities).

and it seems to be due to the use of the orbital dipole as the calibrator.

Table 2. Statistical and systematic uncertainties on the dipole calibration, for single detectors from the lower-frequency HFI channels.

Frequency [GHz]	Statistical error [%]	Systematic (worst case) [%]	Systematic [%]
100	0.004	0.64	0.37
143	0.002	0.53	0.29
217	0.002	0.69	0.41
353	0.010	2.53	1.81

Notes. The "worst case" column corresponds to a situation with a poorly matched sky template, whereas the third column is for the best case. In addition to each of these values, one has to take into account the WMAP solar dipole amplitude uncertainty, 0.24%, as this measurement is our primary calibrator.

We showed in Tristram et al. (2011) that calibration errors induce large-scale features in the Q and U Stokes parameter maps. When using the orbital-dipole-based calibration factors to build these maps, we indeed observe such large-scale patterns, which is further evidence that the latter factors are biased. We also observed a noticeable residual dipole in the reconstructed detector maps, after subtraction of the WMAP measured dipole, for the detectors where the difference between the solar and orbital dipole calibration was larger. We therefore conclude that, in the absence of an accurate correction for the ADC non-linearities, the orbital-dipole calibration scheme cannot be used to calibrate the HFI data.

3.4. Dipole calibration pipeline

We used the `bogopix` results only as to measure the *relative* gain variations, by normalizing to 1 on average between rings 2000 and 6000 (where the solar dipole calibration is computed). We show as an example a compilation of the relative gains reconstructed for the 100, 143, and 217 GHz detectors in Fig. 7. The absolute calibration scale of the CMB channels (100–353 GHz) is set by the solar dipole calibration, as in the HFI early data release (Planck HFI Core Team 2011a), which relied on WMAP solar dipole measurements (Hinshaw et al. 2009).

As a first example of the improvements that `bogopix` provides, we show in Fig. 8 the survey-difference maps (Survey 3 minus Survey 1, and Survey 4 minus Survey 2), for the detector used for Fig. 1. The differences obtained using `bogopix` are lower than $\sim 10\,\mu{\rm K_{CMB}}$ outside the Galactic plane. The remaining residuals in that region, in particular in the Survey 3−Survey 1 difference, can be attributed to the nonlinear nature of the systematic error, only the first-order linear part of which is handled by `bogopix`.

For frequencies ≥353 GHz, `bogopix` results are not reliable, mainly because of the large spatial variation of the sky emission inside a pixel (we have used 1.72′ pixels here). Therefore, we do not correct the highest-frequency channels for any gain variations. This leads to calibration uncertainties of about 1% between maps from individual surveys.

3.5. Dipole calibration uncertainties for single detector

For the dipole calibration scheme, the statistical uncertainties are estimated by propagating the TOI sample variances (NET) to the ring-by-ring gain estimation on the solar dipole, averaged between rings 2000 and 6000, for each detector. These uncertainties are much lower than the systematic uncertainties that

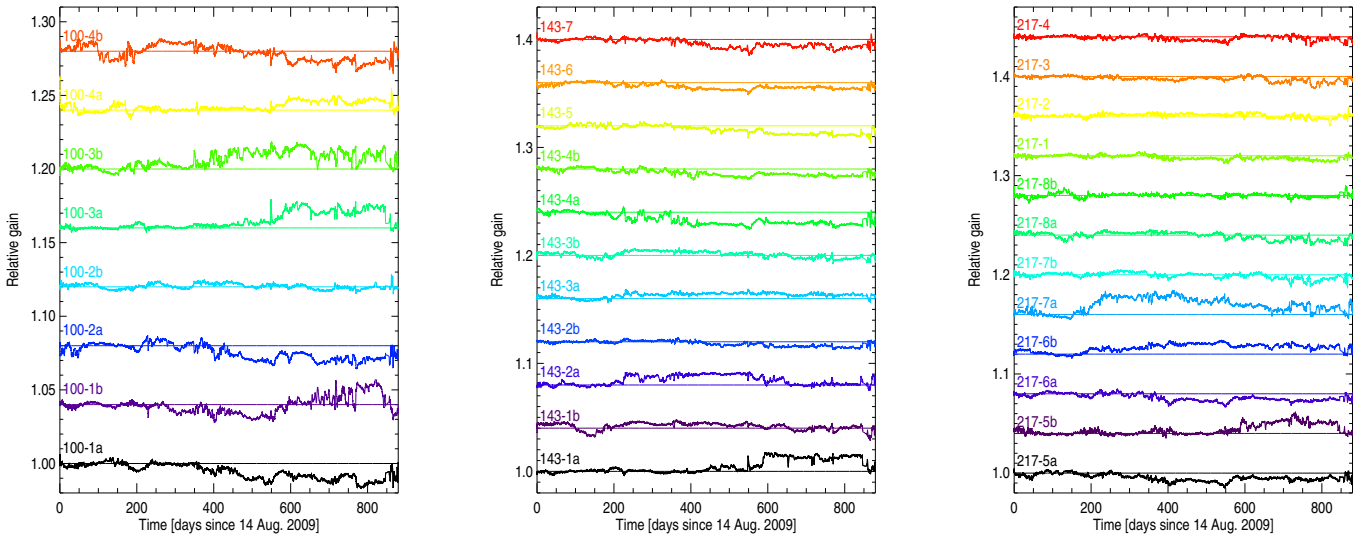

Fig. 7. Relative gains reconstructed by `bogopix` for the 100, 143, and 217 GHz detectors as a function of time, smoothed with a width of 50 rings (about 2 days). Their overall amplitudes are of order 1 to 2%, but both slow and fast (over a few tens of rings, i.e., a day) variations are observed. These variations are largely independent from one detector to the other. Relative gains for each detector have been vertically displaced by 3% for clarity.

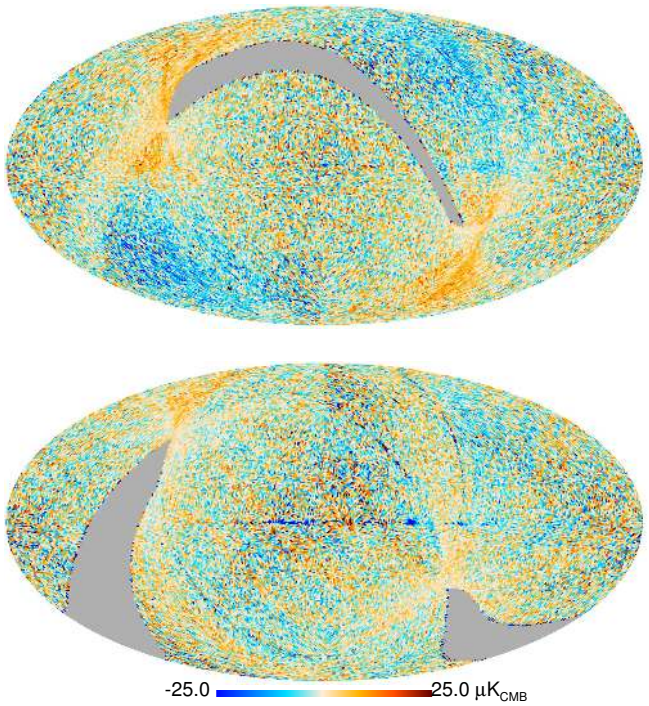

Fig. 8. Residual differences between temperature maps built using data from detector 143-1a, for Surveys 1 and 3 (*top*) and Surveys 2 and 4 (*bottom*), derived using the `bogopix` results. The level of differences is much lower than in Fig. 1.

dominate our calibration measurement. We estimate the size of these systematic uncertainties on the calibration of individual detectors by measuring the dispersion of these ring-by-ring gains. Both uncertainties are listed in Table 2, which gives their average at each frequency. The WMAP solar dipole amplitude uncertainty (0.24%, Hinshaw et al. 2009) is not included. The systematic errors given here should be considered as upper limits on the real systematics, as they have been derived from solar dipole ring-by-ring gains prior to the `bogopix` correction. We indicate the effect of the choice of a Galactic template by indicating a "worst case" scenario (second column of Table 2) in which a non-optimal template was used (see Appendix B for details). When combining different detectors, some of these systematic errors should partially average out for temperature. The gain variation part, for example, is independent from one detector to another. To get a more precise estimation of the calibration accuracy for the frequency maps of this release, we have performed more elaborate tests, which are presented in Sect. 6.

4. Photometric calibration of the high-frequency channels

4.1. From FIRAS-based to planet-based absolute calibration

Since the early days of the *Planck* data, it has been apparent that the ratio between HFI and FIRAS is not constant across the sky: we observe spatial gain variations, i.e., variation of the calibration coefficient K, and thus variation of the offset O (see Eq. (C.3)), that mimic a decrease of K with brightness[2]. Comparison with the dipole calibration at 353 GHz showed that the high-latitude gradients ($10° < |b| < 60°$) give a better agreement. This was thus adopted for the calibration of the *Planck* early results (Planck HFI Core Team 2011b). We studied this unresolved discrepancy with the FIRAS maps further while preparing the first major release of *Planck* data. As detailed in Appendix C, numerous tests and checks have been conducted. However, we could not find any remaining HFI systematics, or any bias in our method of comparison of the two data sets, that could explain such a discrepancy. The only possibility comes from a systematic bias in the FIRAS "pass4" interstellar dust spectra. Indeed, Liang et al. (2012) propose significant revisions to the FIRAS dust spectra that that would reduce the discrepancy with HFI (see their Fig. 1).

In parallel, indications have come to light of an overestimate of the HFI brightness at high frequencies, when calibrating using FIRAS (see Sect. C.5). These have led us to adopt a new

[2] These should not be confused with the apparent gain variation with time, discussed in Sect. 3.1.

photometric calibration scheme for the sub-millimetre channels. We now compare planet flux-density measurements at 545 and 857 GHz with models in order to set the absolute calibration. The ultimate scheme would be to intercalibrate the 545 and 857 GHz channels with the lower-frequency channels, using the planet models as relative calibrators. Indeed, for the Neptune and Uranus planet models used for the calibration, the absolute scale of the model is known to about 5%, whereas the relative inter-frequency uncertainty is expected to be of order of 2% (Moreno 2010). In this section we present our calibration procedure for the 2013 data release.

4.2. Planet flux densities: measurements and comparison with the models

Planck observes the five outer planets: Mars, Jupiter, Saturn, Uranus, and Neptune. The 21 planet observations made by *Planck*-HFI in the whole mission have been analyzed. For calibration purposes, only Neptune and Uranus are used because

(i) Jupiter data lie partly in the nonlinear regime of the HFI read-out system,
(ii) Jupiter and Saturn have strong absorption features that make comparison with the broad-band measurements difficult,
(iii) Mars's flux varies strongly from season to season.

Even though this last issue can be handled precisely by the models, it complicates the analysis, so we defer the use of Mars to future work. For the present data release we applied correction factors to the FIRAS-based calibration coefficients to match the Uranus and Neptune flux densities given by the Moreno (2010) model.

4.2.1. HFI beams and solid angles

The HFI beam solid angles used in this analysis are those derived from Mars observations. We do not use solid angles from the beams that are averaged over the scanning history (the so-called *effective* beams, Planck Collaboration VII 2014), because we consider each observation of Uranus and Neptune for each bolometer separately, and therefore we do not need to compute an average point spread function. We correct for the small response at large scales (more than 40′ from the beam centroid) that is due to incomplete deconvolution of the bolometer/readout electronics time response, as measured on Jupiter. Details of the beam solid angle measurements are given in Planck Collaboration VII (2014).

The beam solid angle is frequency-dependent and its measured value thus depends on the SED of the source. The solid angle for a planet (with a SED roughly proportional to ν^2) is different from that for the photometric convention νI_ν = constant. Maffei et al. (2010) and Tauber et al. (2010) investigated the variation of the beam size across the passband using a pre-launch telescope model. For the lowest frequency HFI bands 100, 143, and 217 GHz, the beam size reaches a minimum near the centre of the band, making the solid angle a weak function of the source's SED. The beam colour corrections for these bands are expected to be less than 0.3%. At 353 GHz the solid angle increases with frequency across the band, but the beam colour corrections are expected to be less than 1%. The multi-moded horns at 545 and 857 GHz are more difficult to model because of uncertainty in the relative phase and amplitudes of the modes propagating through each horn. The models of Murphy et al. (2010) give upper limits on the beam colour correction to the solid angles of 2% at 545 GHz and 1% at 857 GHz.

The FWHM of the beam on the sky is defined by the energy distribution at the entrance of the horn, which – owing to the optical design of the *Planck* telescope – does not depend much on the frequency within the band. The throats of the horns are positioned very close to the focal plane of the telescope, with a deviation varying from horn to horn. If the deviation is small, the variation of the beam solid angle on the sky will be symmetric around the centre of the band, and the combined correction will be small. On the other hand, if the horn is significantly offset, the variation will not be symmetric, and the correction will be larger. An estimate of the correction is presented in Planck Collaboration VII (2014).

The variation of the solid angle inside the band is negligible compared to the error we have on the photometry, and for now the beam solid angle variation for the high-frequency channels has not been taken into account in the calibration. The low variation of resolution across the passband is unusual for a sub-millimetre experiment. By way of comparison, in SPIRE on *Herschel* the FWHM varies by ±17%. The SPIRE beam solid angles have been measured on Neptune; using the photometric convention νI_ν = constant, the corrections to the beam solid angles are about 3.3% at 350 μm and and 5.9% 500 μm (Griffin et al., in prep.).

4.2.2. Uranus and Neptune flux measurements and model comparison

Our calibration procedure follows the following steps:

- A first photometric calibration was set using FIRAS at 545 and 857 GHz.
- We created 2° × 2° maps with a 2′ pixel size around the planet positions by projecting the destriped and calibrated timelines, using the nearest grid point algorithm, from timelines scanning each planet.
- We built maps of the same sky area, using observations taken at different epochs (when the planet was at a different position) to estimate the sky background, and subtracted them from the planet maps. At $\nu \leq 353$ GHz, the background is negligible. At 857 GHz, the astrophysical background is a few percent of the peak signal of Neptune.
- We measured the planet flux densities using aperture photometry on the background-subtracted maps. We integrated the flux up to $3 \times FWHM$. We corrected for the beam solid-angle difference between this scale and the full solid angle. This correction amounts to 0.8% at 545 GHz and 1.5% at 857 GHz.
- At 545 and 857 GHz, we applied a correction factor to the FIRAS calibration to match the Uranus and Neptune flux densities given by the models. The factors were the same for all bolometers within a frequency channel, namely 1.07 at 857 GHz and 1.15 at 545 GHz.

The measurements are colour-corrected (using Eqs. (A.1) and (A.2)) and the flux densities are quoted for the two planet spectra. Colour corrections vary from about 0.92 (at 353 GHz) to 1.05 (at 143 GHz). In the sub-millimetre channels they are <2% at 857 GHz and about 5% at 545 GHz. Errors on the colour corrections are estimated to be 0.25, 0.06, 0.01, 0.006, 0.003 and 0.002% from 100 to 857 GHz (Planck Collaboration IX 2014).

From the flux densities and the planet solid angles estimated for HFI at the date of the observations, we can compute the brightness temperatures T_B. They are given in Table 3, where

Table 3. Neptune and Uranus brightness temperatures measured by HFI.

Frequencies [GHz]	Uranus T_B [K]	Neptune T_B [K]
100	124.3 ± 5.0	129 ± 15
143	108.4 ± 2.9	110 ± 6
217	97.0 ± 2.5	96.9 ± 3.7
353	83.3 ± 2.3	81.1 ± 2.7
545	(73.7 ± 2.4)	(71.2 ± 2.1)
857	(67.5 ± 1.3)	(65.0 ± 1.9)

Notes. At 545 and 857 GHz the numbers are not independent measurements of the planet flux densities, since the data have been recalibrated to match the models.

we averaged the flux densities computed for all detectors in a channel, and all observations' epochs (four), prior to the computation of T_B. The quoted error on T_B comes from the standard deviation of the flux-density measurements.

We use the models called ESA2 for Uranus and ESA3 for Neptune developed by R. Moreno for the *Herschel*-SPIRE absolute photometric calibration (Moreno 2010). The millimetre and sub-millimetre spectra of Uranus and Neptune were modelled with a line-by-line radiative transfer code accounting for the spherical geometry of their planetary atmospheres, like that described for Titan by Moreno et al. (2011). Atmospheric opacity due to the minor species CO (for Neptune only), and NH_3 far wings, as well as collision-induced opacities of the main species (H_2, He, CH_4) were included. The thermal profiles in the troposphere, which is the atmospheric region probed between 90 and 900 GHz, were taken from Lindal (1992). The uncertainty of the computed brightness temperature is mainly linked to the uncertainty on the thermal profile with an absolute uncertainty value of 5%. The relative calibration (between frequencies) is expected to be of the order of 2%.

We compute the flux densities using the brightness temperatures from the model and the planet solid angles estimated for HFI at the date of the observations. The model spectra (in Jy) are interpolated onto our bandpass frequencies, and convolved by our bandpass filters to obtain the flux densities as measured by HFI. In Fig. 9 we compare the flux measurements with the models. Error bars on the HFI data points correspond to the standard deviation of the measurements (for all bolometers and all epochs). For the two high frequencies (857 and 545 GHz), the agreement with the model has been forced by our calibration procedure. For the lower frequencies, calibrated using the dipole, we have an overall very good agreement with the model, the two being compatible within the error bars. Figure 10 shows the same comparison, but on spectra plotted in brightness temperature, and with other measurements from the literature. Notice the high accuracy of the HFI measurements over a wide range of frequencies.

4.3. Planet calibration uncertainties

At high frequencies, we estimate the error on the absolute calibration of the frequency maps to be 10% (for both the 545 and 857 GHz channels). This uncertainty combines the statistical uncertainty in the flux-density measurements (5%) with the systematic uncertainty in the Neptune and Uranus models, taken to be 5%. Note that the latter is probably overestimated as we have a very good relative calibration between the low-frequency channels (143, 217, 353 GHz), which have a much more accurate absolute calibration, and the high-frequency ones.

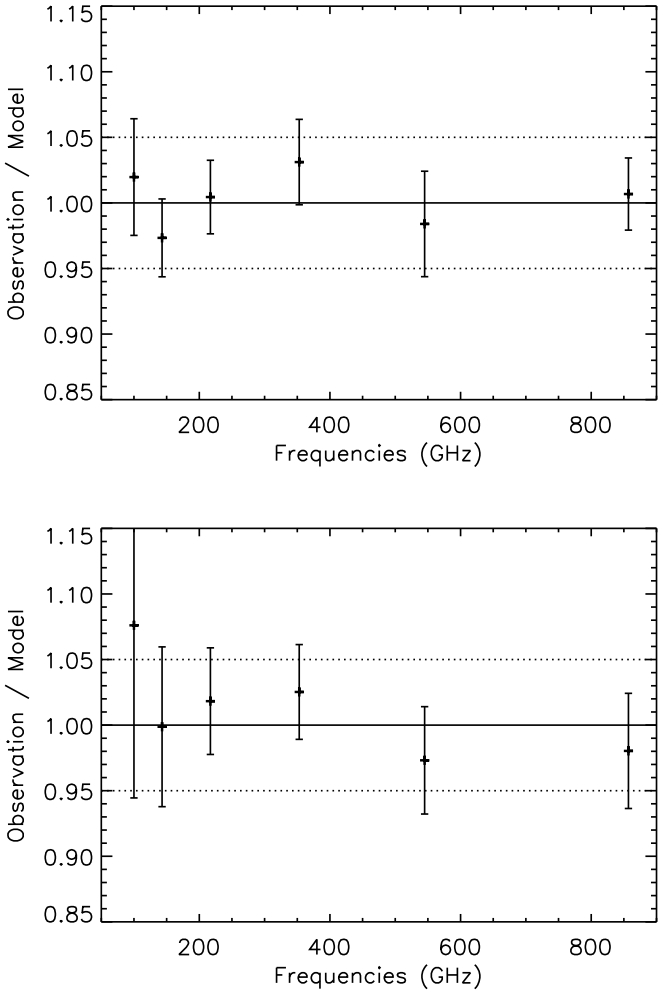

Fig. 9. Ratio of the flux densities measured by HFI and computed from the ESA2 (Uranus, *top*) and ESA3 (Neptune, *bottom*) models from Moreno (2010). At 545 and 857 GHz, the measurements are not independent measurements of the planet flux densities, since the 545 and 857 GHz channels have been re-calibrated to match the average of the Uranus and Neptune flux density given by the models.

5. Setting the zero levels in the maps

At this stage the zero levels of the maps are arbitrary. *Planck* cannot fix them internally and we need to rely on the use of external data sets. The zero level comprises two parts.

1. A Galactic zero level: we estimate the brightness in the *Planck*-HFI maps that corresponds to zero gas column density (zero gas column density means zero Galactic dust emission). As a gas tracer, we use the HI column density (from 21 cm emission), assumed to be a reliable tracer of the Galactic gas column density in very diffuse areas (column density lower than 2×10^{20} cm^{-2} to avoid any contamination by molecular gas).
2. An extragalactic zero level: the cosmic infrared background monopole.

The sum of the two offsets is appropriate for total emission analysis. For Galactic studies, only the Galactic zero level has to be set.

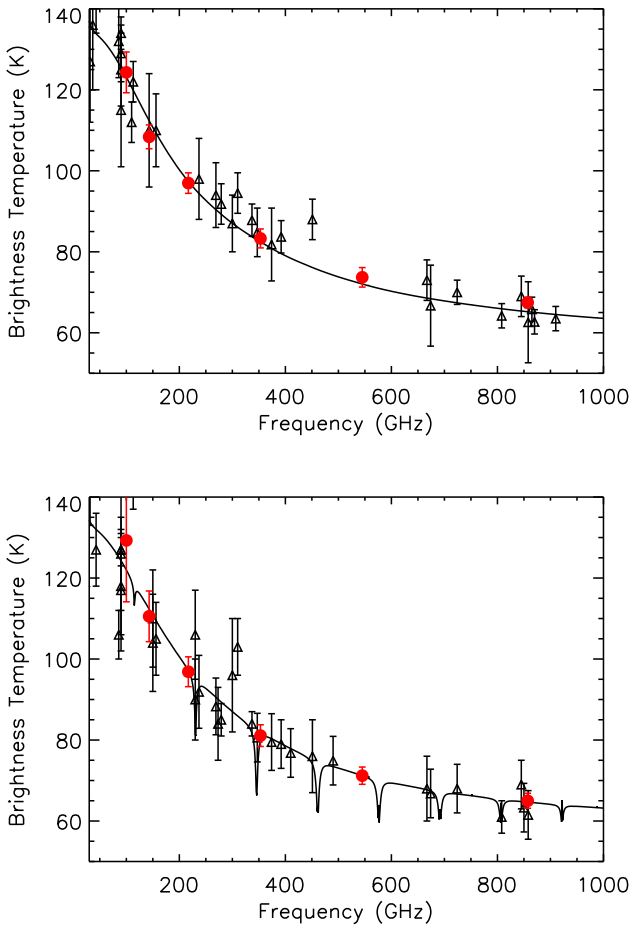

Fig. 10. Variation of brightness temperature with frequency for Uranus (*top*) and Neptune (*bottom*). The brightness temperatures derived from the flux densities measured using aperture photometry on HFI maps are the red points. The continuous lines are the ESA2 (Uranus) and ESA3 (Neptune) models from Moreno (2010). The scale of the models is known at about the 5% level, and the relative inter-frequency uncertainty is expected to be of the order of 2%. At 545 and 857 GHz, the measurements are not independent determinations of the planet flux densities, since the 545 and 857 GHz channels have been re-calibrated to match the average of the Uranus and Neptune flux density given by the models. The other data points are extracted from the literature.

5.1. The Galactic zero level

Two methods have been combined to obtain reliable numbers. The first one uses the correlation of the *Planck* maps with HI column density (following Planck Collaboration XXIV 2011; Planck Collaboration XVIII 2011; Planck Collaboration XXX 2014). The basic idea is to estimate the brightness in the *Planck* maps that corresponds to zero column density by correlating with HI, which is assumed here to be a reliable tracer of the Galactic gas column density in diffuse areas (it thus neglects any dust associated with the diffuse HII gas that is not spatially correlated with the HI). The model is simply

$$I_\nu = \alpha_\nu \times N_{\rm HI} + O_\nu. \quad (7)$$

The correlation with HI allows us to estimate O_ν independently for each frequency, but it relies on the assumption of a tight gas-to-dust correlation over relatively large areas of the sky.

The second method is based on the inter-frequency correlation of *Planck* maps, for which the model is

$$I_\nu = \alpha_\nu \times I_{\nu_0} + O_\nu, \quad (8)$$

with I_{ν_0} being one the *Planck* maps. Here the offsets are all relative to the offset of I_{ν_0} that needs to be determined otherwise (by the first method for instance). The advantage of the second method is that no assumption is made on the phase in which the gas resides (we correlate dust emission with dust emission) and a larger area of the sky can be used to perform the correlation. All the data were smoothed to a common angular resolution of 1°. CMB anisotropies, as extracted in Planck Collaboration XII (2014), were also removed from the data prior to the correlation.

For the correlation with HI, we used the 21-cm all-sky data from the LAB survey (Kalberla et al. 2005). The LAB data are a collection of close to 200 000 spectra that were processed individually. The map of HI column density used here is summed over velocities. The zero level of the LAB data (and of 21 cm observations in general) depends mostly on the baseline subtraction at the spectrum level. At 1420 MHz, the spectroscopic observation is the sum of the 21 cm line, the synchrotron and free-free emissions (which are well approximated by a power law at this frequency), and instrumental baseline variations due to various effects, including ground radio interference and system temperature variations. The 21 cm emission is usually extracted by removing a baseline using a polynomial fit constrained with velocity channels away from the HI Galactic emission. The two radiotelescopes used to build the LAB data have a large velocity range coverage (from −450 to 400 km s^{-1}), necessary for an accurate baseline removal. In addition many sky positions were observed several times, allowing improvement on the baseline correction. Because the baseline correction is applied on each individual spectrum, the noise on the zero level will be at the pixel size on the final map and no bias at large angular scales should be expected. Larger-scale zero-level variations could come from stray (far sidelobe) radiation. However, the LAB data were constructed with the most precise stray-radiation correction to date, leaving very faint residual emission, at a level of 2% (considering Galactic line emission). For the gain calibration, strong radio sources are used (see Kalberla et al. 2005). The calibration is performed regularly during observations to monitor any gain drift. The precision of the gain of the LAB data has no impact on the determination of the HFI zero level, as it is obtained through a correlation.

The first method requires the use of a very strict mask, to include only regions where the gas is mostly in the neutral atomic form (no significant dark gas for example) and avoiding lines of sight with significant emission from clouds in the Galactic halo (intermediate velocity clouds and high velocity clouds), as they have slightly different dust emission properties. We select pixels where the local velocity cloud HI column density is less than 2×10^{20} cm^{-2} and where no significant IVC emission is detected. This very strict mask includes 11.5% of the sky. For inter-frequency correlations (Eq. (8)), a second mask was built by including pixels where the local velocity cloud HI column density is less than 3×10^{20} cm^{-2} (and no restriction on IVCs), increasing the sky fraction to 28%.

To minimize the effect of the imperfect dust-to-HI correlation and to obtain the highest possible signal-to-noise ratio, the Galactic zero levels were computed using Eq. (7) at 857 GHz and using Eq. (8) at the other frequencies, thus taking $I_{\nu_0} = I_{857}$. In Fig. 11 we show the 857 GHz-HI correlation. We observe a significant dispersion in this correlation, possibly due to variations of the dust-to-gas ratio or variations of the dust properties,

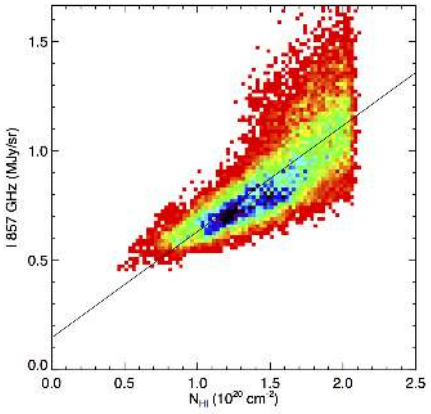

Fig. 11. 857 GHz-HI correlation over 11.5% of the sky ($N_{\rm HI} < 2 \times 10^{20}$ cm^{-2} – smoothed to 1° – and excluding intermediate velocity clouds).

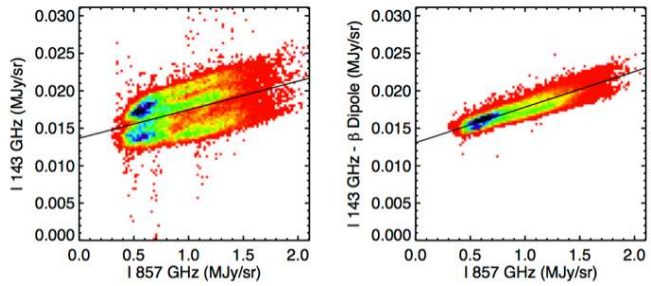

Fig. 12. Correlation between the 143 and 857 GHz frequency maps on 28% of the sky (HI column density smoothed at 1° lower than 3×10^{20} cm^{-2}). CMB anisotropies have been removed at 143 GHz. *Left*: raw correlation. *Right*: correlation after a residual solar dipole has been removed at 143 GHz. The offset of this correlation sets the Galactic zero level of the 143 GHz map.

or due to the fact that HI is not a perfect tracer of column density (e.g., presence of dust in the warm ionized medium). Figure 12 shows an example of inter-frequency correlation, at 143 GHz. Their correlation plots are clearly split in two, revealing an effect unaccounted for in our model (Eq. (8)). Once projected onto the sky, the residual shows that the north and south parts of the mask have different offset values. This bi-modal structure is minimized once a residual solar dipole is removed from the data. To set the Galactic zero level, we therefore also fit for the amplitude of an additional residual solar dipole term in Eq. (8). The amplitude of this residual dipole pattern is in accordance with the actual accuracy of the absolute calibration (discussed in Sect 3.5). Indeed, with a given accuracy on the absolute calibration, a dipole with an amplitude of at least the given accuracy can be left in the map. There is no contradiction between the amplitude of the dipole left in the maps and the current absolute calibration uncertainties, listed in Table 11. More precisely, we found residual dipole amplitudes compatible with a 0.3% calibration error for 100–217 GHz and 1% for 353 GHz.

5.2. The cosmic infrared background monopole

The (isotropic) mean value of the CIB is computed using the Béthermin et al. (2012) model. This is an empirical model based on the current understanding of the evolution of main-sequence and starburst galaxies. It reproduces the mid-infrared to radio galaxy counts very well. The values of the CIB (which is the integral of the emission from galaxies) have been computed using the HFI bandpass filters. They have then been converted into the convention νI_ν = constant using the CIB SED fit of Gispert et al. (2000). The values are given in Table 4. They are consistent with those extracted from FIRAS data (see Table C.2). Errors are on the order of 20%. The CIB has to be added to the maps for total emission analysis.

Table 4. CIB monopole that has to be added to the maps.

Frequencies [GHz]	CIB [MJy sr^{-1}] (νI_ν = constant)
100	3.0×10^{-3}
143	7.9×10^{-3}
217	3.3×10^{-2}
353	1.3×10^{-1}
545	3.5×10^{-1}
857	6.4×10^{-1}

Table 5. Offsets that have to be removed at each frequency to set the Galactic zero level.

Frequencies [GHz]	Total maps [MJy sr^{-1}] (νI_ν = constant)	Zodi-removed maps [MJy sr^{-1}] (νI_ν = constant)
100	0.0047 ± 0.0008	0.0044 ± 0.0009
143	0.0136 ± 0.0010	0.0139 ± 0.0010
217	0.0384 ± 0.0024	0.0392 ± 0.0023
353	0.0885 ± 0.0067	0.0851 ± 0.0058
545	0.1065 ± 0.0165	0.0947 ± 0.0140
857	0.1470 ± 0.0147	0.0929 ± 0.0093

Notes. These offsets have been computed assuming zero Galactic dust emission for zero gas column density.

5.3. Set the appropriate zero levels of HFI maps

For Galactic analysis, the Galactic zero levels, given in Table 5, have to be removed from the frequency maps in the 2013 data release . For total emission analysis, the CIB monopole, given in Table 4, has furthermore to be added. As stated previously, for the CIB we estimate the error to be of the order of 20%. For the Galactic zero level, errors are given in Table 5. The uncertainty on the 857 GHz Galactic offset is dominated by systematics. At lower frequencies, the uncertainties take into account the impact of the CMB removal, the statistical uncertainty of the fit, and the error on the 857 GHz offset.

6. Characterization and checks of calibration

In this section we present the various tests that have been carried out to assess the precision and stability of the calibration of the HFI data.

6.1. Time stability of the calibration

To evaluate the accuracy of the apparent gain variation correction coming from `bogopix` we compute, for each detector, the residual difference R between the HPR data d and a model including the destriping offsets o_r, the HFI I, Q and U maps, the dipoles $t_{\rm D}$ (orbital and solar) and the calibration parameters (relative ring-by-ring gains g_r from `bogopix`, overall gain $\tilde{G}^{\rm SD}$ based on the solar dipole, and zero point z derived as described

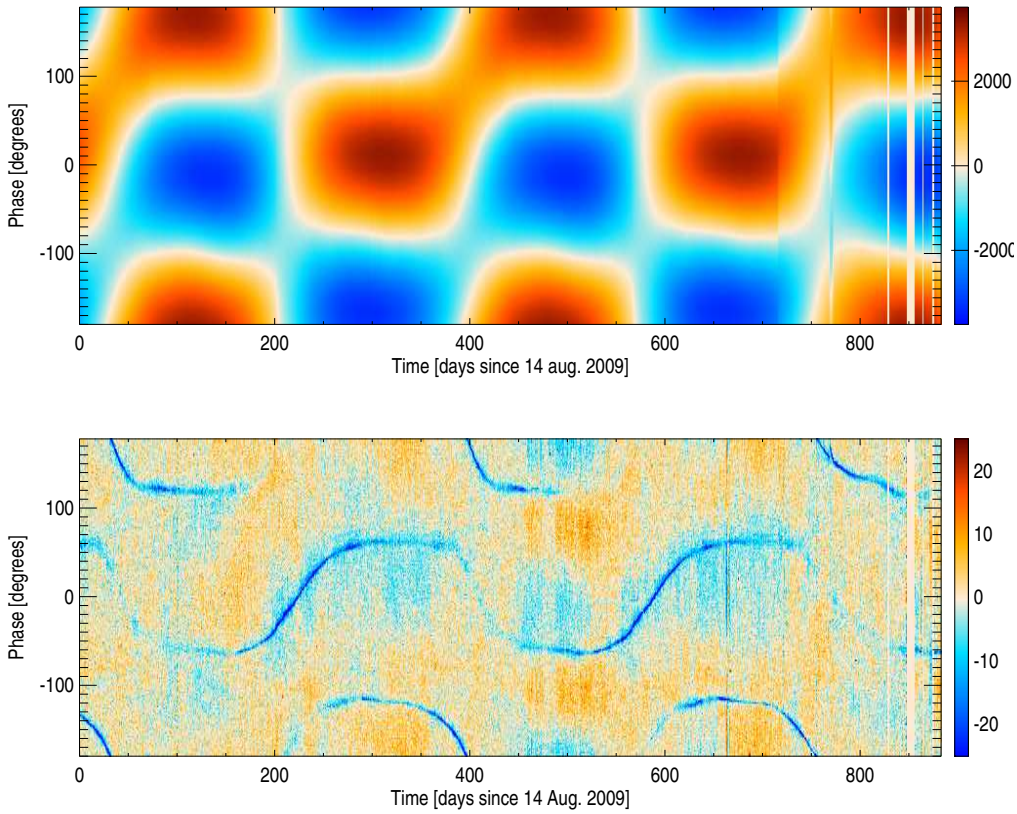

Fig. 13. *Bottom*: distribution of the residuals in μK_{CMB}, computed using Eq. (9), for detector 143-1a, plotted versus observation date and satellite rotation phase. *Top*: expected pattern for the solar dipole, in μK_{CMB}. Comparison of the two plots provides a check of the level of residual gain variation after applying the `bogopix` gains. In the residuals the sharp features (dark blue) correspond to the Galaxy observations, where band-pass effects have not been corrected.

above). This corresponds, for each HPR sample i of each ring r, and pixel p to:

$$R_i = (d_i - o_r)/\left(g_r \cdot \tilde{G}^{\rm SD}\right) - t_{\rm D} - I_p - \frac{1-\eta}{1+\eta}\left(Q_p \cos 2\psi_i + U_p \sin 2\psi_i\right) - z. \quad (9)$$

We display these residuals as a function of the rotation phase, i.e., the angle between the direction of the pixel in the HPR and the satellite velocity, in Fig. 13. In this representation, the orbital dipole extrema will be found at fixed phases 0 and $\pm\pi$. The solar dipole will present a modulated pattern, also illustrated in Fig. 13. As the solar dipole is the brightest component of the sky emission, its pattern in the residuals is a good indication of inaccuracy of the gain variation correction. This may also capture additional time variable signals that would not be accounted for in our processing, for example the primary spillover pick-up. The areas where the Galactic emissions dominate show up as outliers in these residuals, for several reasons. First, they correspond to regions were intra-pixel gradients are large, and will leave some imprint due to the individual scanning trajectories of each detector. More importantly, they present emission spectra different from that of the CMB, on which we calibrate. Integrated over each detector's bandpass, this will translate into an apparent brightness difference. At this stage, we do not apply colour corrections to get rid of such effects, considering that they can be minimized by a proper selection of the sky area (i.e., avoiding the Galactic plane). Finally, imperfections in the time response of the detectors and in the pointing reconstruction will also induce larger residuals in the Galactic plane. Masking these regions, using a 40% Galactic mask, we checked that, for all the 100−217 GHz detectors, the maximum level of the residuals we observe would correspond to a remaining gain variation lower than 0.3% (i.e., residuals lower than 10 μK_{CMB}).

6.2. Intra-frequency calibration checks

We have checked the relative calibration of the detectors within a given frequency channel using pseudo-cross-power spectra. We start from the single-detector temperature maps, neglecting polarization. We mask sky areas where the Galactic emissions are large, keeping 40% of the sky for frequencies lower than 300 GHz and 30% above. We build the pseudo-cross spectra of this set of maps, using `Xspect` (Tristram et al. 2005). We correct each pseudo-spectrum for its beam window function (Planck Collaboration VII 2014). We then focus on the location of the first acoustic peak, so that results are not biased by beam uncertainties. For example, the set of spectra we obtain for the 143 GHz HFI detectors is shown in Fig. 14. Finally, we fit the recalibration coefficients that minimize the differences between these spectra, for ℓ in the range [25, 300]. For 545 and 857 GHz we apply a colour correction for the band-pass mismatch between detectors, assuming the *IRAS* spectral convention. The relative calibration coefficients found with this method should be considered as upper limits on the relative calibration precision of HFI, as we neglect polarization in this analysis. They are given for all frequencies in Table 6. For frequencies below 217 GHz the relative calibration accuracy is better than 0.4%.

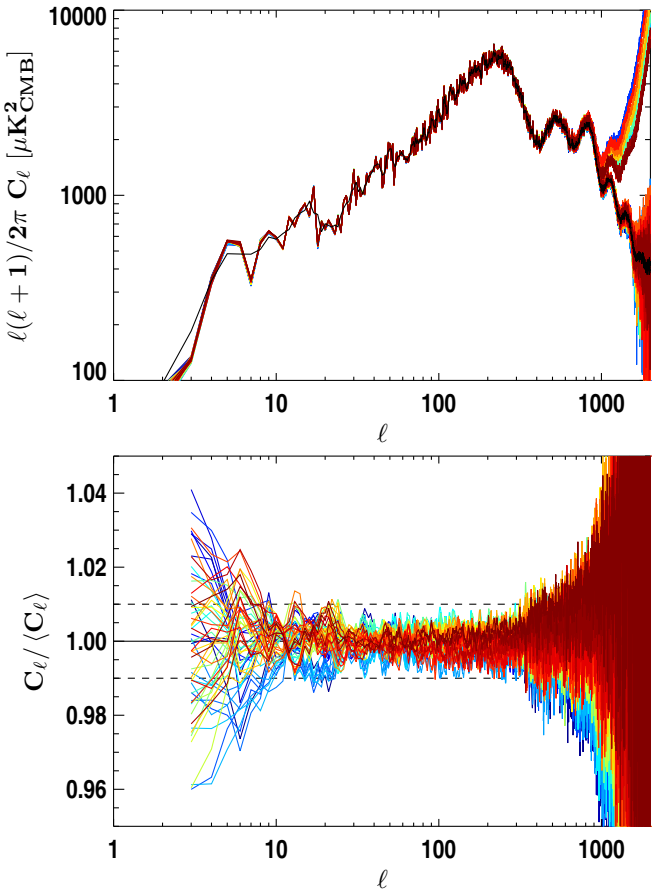

Fig. 14. Auto- and pseudo-cross-spectra obtained from the eleven 143 GHz HFI detectors corrected for the beam (*top*) and their ratio with respect to the average of the pseudo-cross-spectra (*bottom*). This average is indicated in black in the top panel. Each detector pair is shown in a different colour. Note the noise suppression in the cross-spectra above $\ell \sim 800$.

Table 6. Maximum absolute value of the relative calibration coefficients fitted on pseudo-spectra similar to those of Fig. 14, between detectors of each frequency.

Frequency [GHz]	100	143	217	353	545	857
Calibration [%]	0.39	0.28	0.21	1.35	1.3	1.4

Notes. These values are upper limits on the relative calibration errors within each channel (i.e., between all bolometers of a given channel).

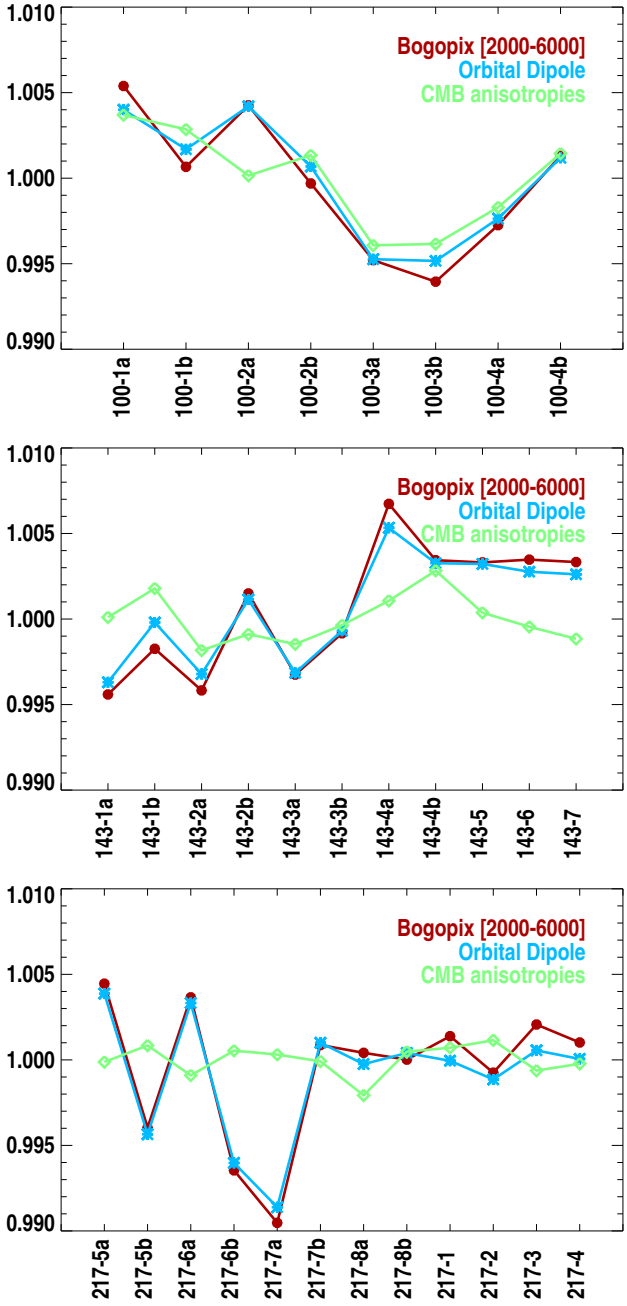

Fig. 15. Relative calibration coefficients found when calibrating on the orbital dipole (constant gain, light blue, with `bogopix` in red) and using CMB anisotropies (see Sect. 6.2, in green), with respect to the solar dipole gains, used to build the HFI maps. As ADC non-linearities are not corrected for, calibration systematics depend on the amplitude on the signal used to check for them. The amplitudes of such effects are within the systematic uncertainties quoted in Table 6.

These relative accuracies are consistent with the systematic uncertainties estimated in the previous section.

In Fig. 15, we compare the relative calibration coefficients derived from the pseudo-cross spectra, for all 100, 143 and 217 GHz detectors, with the relative differences between gains based on solar and orbital dipole calibration methods (see Sect. 3.3). Both orbital dipole methods are affected by the same systematics, namely the ADC non-linearities. CMB anisotropies are well intercalibrated between detectors, using solar dipole calibration. This reinforces the choice of the solar dipole calibration.

6.3. Inter-frequency and absolute calibration checks for CMB-dominated channels

In this section, we describe the checks performed to study the calibration accuracy for CMB channels.

6.3.1. Pseudo-cross-power spectrum analysis

We applied a technique similar to that presented in Sect. 6.2 to assess the HFI inter-frequency relative calibration for combined maps, at frequencies where the CMB dominates at high Galactic

Table 7. Cross-calibration coefficients that minimize the dispersion of the HFI temperature cross-spectra around their common mean.

Frequency [GHz]	100	143	217
Calibration	1.002	0.999	0.999

Table 8. Differences between the CMB dipole parameters fitted on the HFI maps with those measured by WMAP.

Frequency [GHz]	Amplitude [%]	Longitude [′]	Latitude [′]
100	−0.122	2.30	11.09
143	−0.074	3.00	11.91
217	−0.091	−5.10	12.79

Notes. The typical statistical errors on these fits are ∼0.01% for the amplitude and less than 1′ for the direction.

latitudes. We built pseudo-power spectra from the temperature maps for 100, 143, and 217 GHz, applying the beam correction described in Planck Collaboration VII (2014). As above, we determined the cross-calibration coefficients that minimize the difference between the pseudo-cross-power spectra of the HFI maps for ℓ in the range [25, 300]. Results from this analysis are shown in Table 7. We see from these numbers that the internal relative calibration precision between the 100, 143 and 217 GHz channels is better than 0.15%.

6.3.2. Solar-dipole parameter fits

We also studied the calibration accuracy using fits of the CMB dipole parameters on HFI maps. To perform this test, we used maps built without dipole subtraction. Such fits are likely to be biased in the presence of foregrounds, in particular due to the intrinsic dipole of the Galactic emissions. We therefore used a template fitting method to subtract dust emission; our dust template is based on *IRAS* data (Neugebauer et al. 1984). We masked 10% of the sky, based on Galactic dust and CO emission, as well as point sources, before fitting the amplitude and direction of the CMB dipole. We recover the WMAP dipole amplitude measurement at the level of 0.1% or better in all cases (Table 8). The direction, perhaps more affected by foreground residuals or by uncertainties in the time response, is reconstructed within about 10′. These results are in agreement with the residual dipole measurements presented in Sect. 5.1, which might be more sensitive to foreground removal and masking.

6.3.3. Calibration checks using component separation methods

Finally, calibration consistency checks have been performed using component separation tools. In particular, the SMICA component separation method (Cardoso et al. 2008) has been used to fit relative calibration coefficients for each frequency (including LFI data) on the CMB anisotropies (Planck Collaboration XII 2014). The foreground model is a non-parametric 4-dimensional model, meaning that the foregrounds are represented by four templates with arbitrary emission laws, arbitrary angular spectra, and arbitrary correlations (2- and 3-dimensional fits were also performed with compatible results). Relative-calibration coefficients between frequency power spectra obtained using this method are summarized in Table 9. They agree, within errors,

Table 9. Cross-calibration coefficients of the HFI sky maps at each frequency, with respect to the 143 GHz map, found with the SMICA component separation method, with errors derived from a Fisher matrix analysis.

Frequency [GHz]	Relative calibration –	Fisher errors [%]
100	0.999	0.2
143	1	0.2
217	1.000	0.2
353	0.993	0.3
545	1.05	3.5

with the results shown in Tables 7 and 8. It should be noted that for frequencies >353 GHz, Rayleigh scattering, not included in such studies, will distort the CMB anisotropies used to derive such cross-calibrations, at the few percent level (Yu et al. 2001). Therefore cross-calibration coefficients found for 353 and 545 GHz, which are of the same order, should be considered as estimates of systematic cross-calibration uncertainties, rather than genuine corrections of our maps. Such studies are routinely incorporated in *Planck* likelihood minimizations (Planck Collaboration XV 2014), and more results are shown in Planck Collaboration XV (2014). Comparisons with LFI and WMAP are presented in Planck Collaboration XVI (2014).

6.4. HFI/SPIRE cross-calibration on diffuse emission

At high frequency, uncertainties in the SEDs of the astrophysical components, together with their variation across the sky, make extensive calibration checks as performed in Sect. 6.1 and 6.3 more difficult. However, we can study the cross-calibration between HFI and other data sets, like *Herschel*-SPIRE (Griffin et al. 2010). HFI and SPIRE have two very close frequency channels: 857 GHz for *Planck* versus 350 μm (857 GHz) for SPIRE, and 545 GHz versus 500 μm (600 GHz). To compare the HFI and SPIRE brightness, we used nine large SPIRE public Galactic fields (for a total of about 75 deg^2), with mean brightness ranging from 1.8 to 285 MJy sr^{-1} at 857 GHz.

For each field we create SPIRE 350 and 500 μm maps using the Herschel Interactive Processing Environment pipeline HIPE v9.1. We applied the relative gain correction for extended emission and used the destriper module. SPIRE data are calibrated using Neptune and are given in Jy beam^{-1} for the convention νI_ν = constant. To convert the point source calibration to an extended emission calibration, we use the SPIRE beam solid angles of 822 arcsec^2 and 1768 arcsec^2 at 350 and 500 μm respectively.[3] These values are also derived using the νI_ν = constant convention. SPIRE maps are then convolved with the HFI beam window function.

To compute the colour corrections, we use the SPIRE Relative Spectral Response Functions (RSRFs)[4]. The SPIRE beam FWHM values vary as ν^γ with frequency, where $\gamma = 0.85$ at both 350 and 500 μm (Griffin et al., in prep.). To take this effect into account, we multiply the SPIRE RSRFs by $\nu^{-2\gamma}$ and renormalize them. Colour-correction factors, to convert SPIRE monochromatic flux densities into HFI-like monochromatic flux densities, are computed assuming the real source spectrum is a

[3] https://nhscsci.ipac.caltech.edu/sc/index.php/Spire/PhotBeamProfileDataAndAnalysis

[4] https://nhscsci.ipac.caltech.edu/sc/index.php/Spire/PhotInstrumentDescription

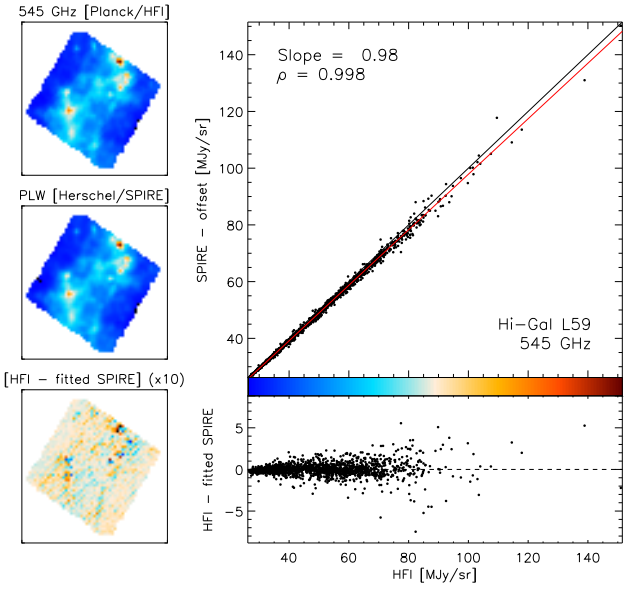

Fig. 16. SPIRE/HFI pixel-to-pixel comparison at 545 GHz in one 6.3 deg^2 field from the Herschel infrared Galactic Plane Survey (Molinari et al. 2010). The red line is the result of a linear fit while the black line has a slope of unity. On the left are shown the HFI and SPIRE maps, together with the difference of the two. The difference is displayed between −6.3 and 6.3 MJy sr^{-1}.

modified blackbody of a given temperature and emissivity index: $B_\nu(T) \times \nu^\beta$. The temperature T and emissivity index β are taken from the full-sky T and β maps available in the *Planck* Legacy Archive.

We estimate the agreement between the diffuse emission measurements from HFI and SPIRE by computing their correlation. An example of a scatter plot for one field and one frequency is shown in Fig 16. In all fields, HFI and SPIRE measurements correlate very well, with an average Pearson correlation coefficient of 0.998. The dispersion across the linear fit ranges from about 2% to 8% of the mean brightness of the field. The SPIRE/HFI gain ratios are 0.972 at 545 and 0.936 at 857 GHz. At 545 GHz, the agreement between the HFI and SPIRE absolute calibration is very good. At 857 GHz, we observe a systematic trend, with SPIRE being lower than HFI by 6.4%. This difference is just within the joint uncertainties of the absolute calibration of the two instruments, which are 5% for HFI (see Sect. 4.3), and 2% for SPIRE (see SPIRE observer manual[5]), putting aside the 5% systematic uncertainty of the Planet's models. We note however that the version of the SPIRE pipeline that was used for this comparison was based on the Neptune ESA2 model whereas HFI used the ESA3 model, which is of order 1.5% higher over the frequency range of interest. Moreover, contrary to SPIRE, we also use Uranus to calibrate. Considering these additional sources of bias to the relative HFI-to-SPIRE calibration, we are not unduly worried about the current difference between HFI and SPIRE at 857 GHz.

6.5. Map noise level assessment

When combining detector data to build frequency maps, we apply an inverse noise weighting scheme. The weights we use are derived from the noise levels measured from clean TOIs together with the calibration coefficients. The resulting noise level in the combined maps is therefore a consistency check of the relative calibration between detectors, since a mis-calibration would result in additional noise, given the slightly different scanning path and redundancies of the detectors.

In Fig. 17 we show the intensity maps constructed for each of the HFI frequencies, together with the number of TOI samples per pixel; and difference-maps built with the first and second half of each rings, both as the raw differences, and as differences scaled by the square root of the number of TOI samples to prewhiten them.

The detector noise estimate used for the detector's data weighting is slightly different for the 2013 data release than for the previous release (Planck HFI Core Team 2011b). As a consequence, the pixel covariances we compute are now consistent with noise levels estimated from the difference maps built from the first and second half of the rings.

Figure 18 presents pseudo-spectra of the null test difference maps, computed with a 15% Galactic mask for frequencies up to 353 GHz, or 40% for the higher frequencies, combined with a point source mask derived from the *Planck* catalogue of compact sources (Planck Collaboration XXVIII 2014). We compare these spectra in Fig. 18 with those from the half-difference of the maps reconstructed from Surveys 1 and 2, properly normalized to compensate for the lower integration time. As illustrated previously, in Fig. 1, such differences are sensitive to, among other things, time variations in the gains. As they compare observations made with roughly opposite scan directions, they may also exhibit residuals in regions where the sky signal is intense, and large gradients due to imperfect deconvolution of time response (Planck Collaboration VI 2014). As a consequence, their spectra, shown as dashed lines in Fig. 18, are higher at low multipoles than those of the half-ring differences. The fact that both half-difference spectra are very close to each other at high multipoles for frequencies lower than 353 GHz is an indication that these differences provide an estimate of the high spatial-frequency part of the noise included in the HFI 2013 data release. For the submillimetre channels, both spectra present a significant ℓ variation, showing that they are contaminated by systematic residuals.

From these pseudo-spectra we estimate the noise level in the HFI maps by computing their average, after re-normalization by the sky coverage, in the ℓ range 100−6000. Using the averaged hit count per pixel, we convert these averages into an equivalent rms per TOI sample. We compare this estimate with two others: the rms of the half-ring map differences, properly whitened using the hit counts; and the averaged square-root of the variance computed in each pixel by the projection module, scaled to a dispersion per TOI sample using the averaged hit counts. These estimates are compared in Table 10. In general, they are in fair agreement for the three lowest frequencies, indicating that they are a good estimate of the noise level in the maps. At higher frequencies, however, signal residuals give a larger contributions. Therefore, such methods only provide an upper limit on the high-frequency noise in the maps.

7. Conclusions

In this paper we have presented the mapmaking and calibration procedures used for the *Planck* HFI data in the 2013 release. The calibrator for the CMB frequency data (100−353 GHz) is the solar dipole anisotropy as measured by WMAP (Hinshaw et al. 2009). This calibration is performed through a ring-by-ring template fit. Its limitations are largely a consequence of the

[5] http://herschel.esac.esa.int/Docs/SPIRE/html/spire_om.html

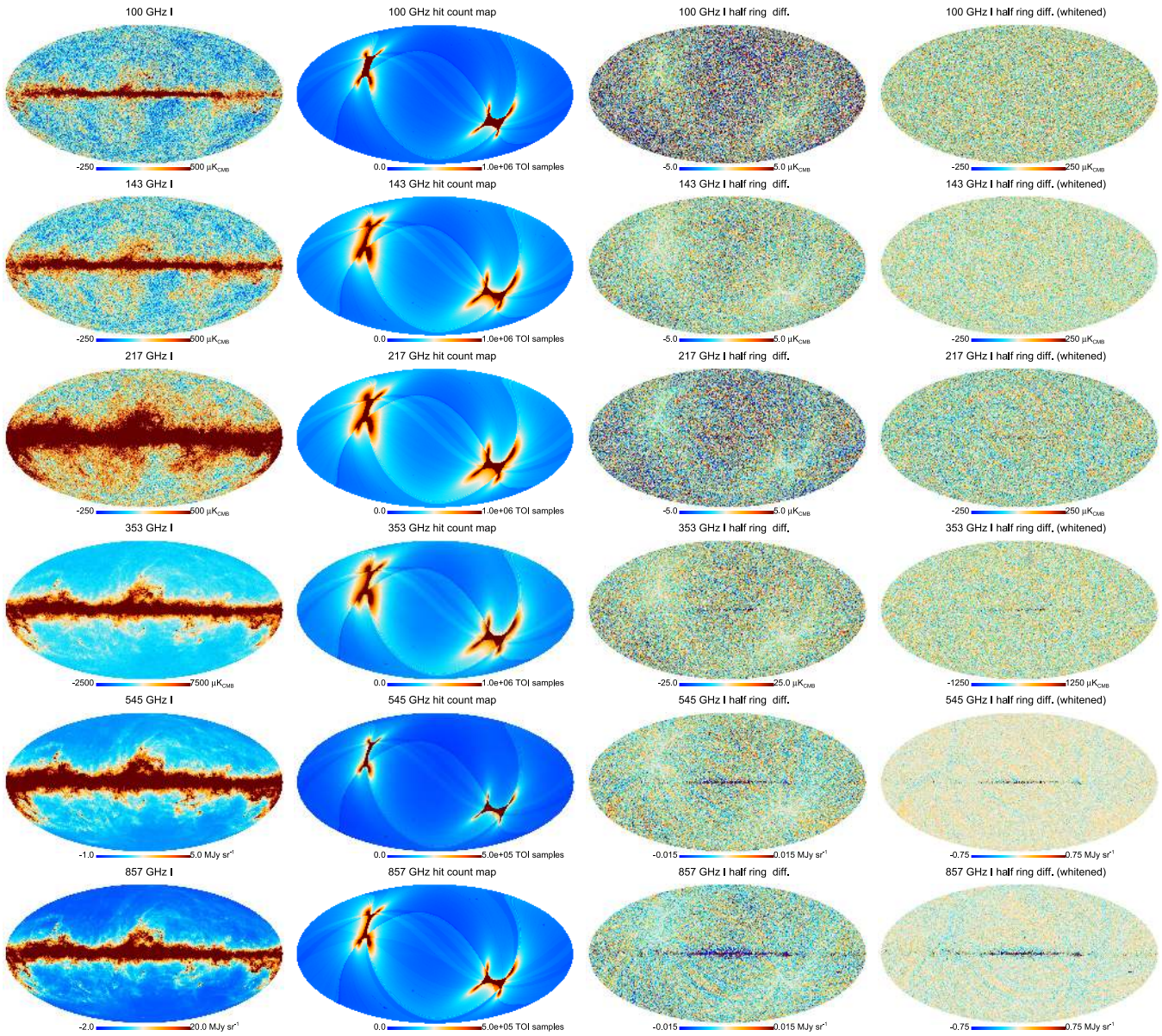

Fig. 17. Signal (*left*), hit counts (second column) and half differences between maps built with only the first and second half of each ring (third column) for all HFI frequencies. The half ring differences are clearly correlated with the hit count maps. The last column shows the half-ring difference maps, scaled by the square root of the number of TOI samples, which largely removes this correlation. For the two highest frequencies, the differences show residual stripes and signal artefacts, at a low level (below 1% of the sky signal). The difference maps have been degraded to Nside = 128 `HEALPix` resolution.

non-ideal behaviour of the ADC from the bolometer read-out electronics. Tiny deviations from linearity in these devices cause apparent gain variation of the detector chain with time, which we have addressed using an effective gain correction, `bogopix`. We showed that this scheme reduces the apparent gain variation in time from 1−2% to lower than 0.3%, by studying the residuals of the map built for different time. Higher-order signal distortions induced by this systematic effect prevent us from using the more precise, orbital dipole-based calibration scheme presented in Tristram et al. (2011).

Correction for the ADC non-linearities should be made prior to any data reduction step. It requires precise measurements of each ADC response, which is currently taking place using data from the warm (4K) instrument. First tests of systematic corrections are also under way, with promising results. The time transfer functions used to deconvolve the data are derived from planets and galactic plane observations. These observations are not sensitive to time constant longer than 1 s, that are observed by studying the thermal behaviour of the bolometers/bolometer plate system (Planck Collaboration II 2011). Such long time constant are shifting significantly the dipoles axis, and could thus affect the data at very low levels (below those of the ADC non-linearities correction), and contribute to the residual level of systematic inconsistencies observed in this paper.

The calibration for the 545 and 857 GHz channels is performed by comparing Uranus and Neptune flux densities with models of their emissivities. We had to switch to this scheme owing to apparent systematic effects in the FIRAS spectra we used in the HFI Early Data release. At those frequencies, time variations of the gain are lower than other systematic calibration uncertainties.

We revised our zero level-setting method, which now relies on the CIB monopole and the zero of the Galactic emission, defined as zero dust emission for a null HI column density.

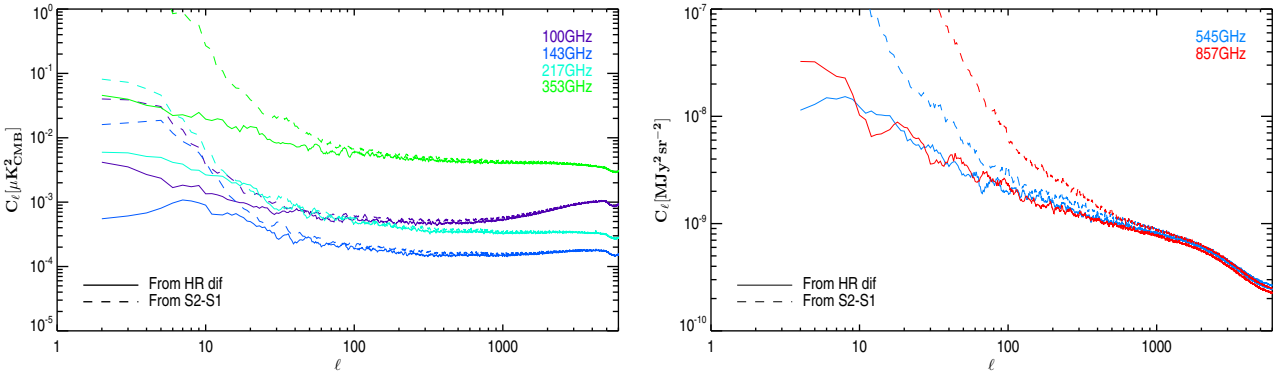

Fig. 18. Pseudo-power spectra reconstructed from the half-differences between maps from the first and the second half of each ring (continuous lines) and the half-differences between maps restricted to Survey 1 and 2 (dashed lines) for, respectively, the dipole calibrated channels (*right*) and the sub-millimetre ones (*right*). These pseudo-spectra were computed using Galactic masks, removing 15% (≤353 GHz) or 40% of the sky (sub-mm channels), combined with the *Planck* point source mask. For high-frequency channels, power spectra are dominated by signal and destriping residuals, due to gradients inside the pixels, which are not scanned at exactly the same positions in the two data sets. In the survey differences, other systematics like time response, pointing drifts, and residual gain variations also induce larger residuals.

Table 10. Results of the three methods for deriving the TOI rms per sample from: (a) the variance maps; (b) the rms of the half ring difference maps; and (c) the pseudo spectra from Fig. 18 (as explained in the text) for each frequency.

Frequency [GHz]	Var. maps (a)	Diff. maps (b)	Spectra (c)	Units
100	1569	1546	1554	μK_{CMB}
143	777	775	826	μK_{CMB}
217	1109	1105	1212	μK_{CMB}
353	3671	3712	4101	μK_{CMB}
545	0.604	0.976	0.817	MJy sr^{-1}
857	0.695	2.58	0.920	MJy sr^{-1}

Notes. Units are μK_{CMB} for 100 to 353 GHz, and MJy sr^{-1} (νI_ν = constant) for the sub-mm channels. These results should be considered as rough estimates only. The higher the frequency, the larger are the contributions of systematics residuals in the half-differences, e.g., time constants and signal gradients.

At all frequencies, the statistical uncertainty of the calibration is negligible compared to the systematic uncertainty. The systematic uncertainty has been evaluated using several methods, presented in Sect. 6. We evaluated three types of systematic uncertainties:

(a) *Residual apparent variations of gains with time*. For the 100 to 217 GHz maps, we showed in Sect. 6.1 that, using `bogopix`, these variations were lower than 0.3%, for each individual detector. As shown in Fig. 7 the gain variations appear to be independent from one detector to the other, so such uncertainties should average out in the combined maps from this release. This 0.3% uncertainty is therefore a conservative upper limit on the level of residual gain variations in the frequency maps. At higher frequencies, no estimation, nor correction for the apparent gain variation, is available. We choose to quote the level of variations we observed in the single detector measurements of `bogopix` at lower frequencies, which is 1%; this is again an upper limit for combined maps. Given *Planck*'s scanning strategy, such uncertainties might be relevant for point-like sources studies, as these are observed in general once per survey, or globally when comparing sky maps from individual surveys.

(b) *Relative calibration uncertainties*, which should be used when combining different frequency maps, e.g., when reconstructing the SED of an object. We presented in Sect. 6.3 several methods to evaluate such uncertainties for 100 to 217 GHz channels. Both a direct comparison of pseudo-power spectra outside the Galaxy and results from the component separation method `SMICA` show that the inter-calibration between the 100, 143, and 217 GHz channels is better than 0.2% (we keep the more conservative estimate, using `SMICA` for the reported errors). We complement these results with the upper limits extracted from `SMICA` at 353 and 545 GHz, using the central value (1 and 5%, respectively) as an upper limit on the uncertainty. For the relative calibration of the 857 GHz maps, we quote the 5% uncertainty on the photometry used in the planet calibration.

(c) *Absolute calibration uncertainties* that should be considered when comparing with other data sets. This involves comparing *Planck* data with an external calibrator. Below 353 GHz, such uncertainties have been evaluated by two complementary approaches: reconstructing the dipole and comparing it with the *WMAP* measurements (Sect. 6.3); and evaluating the amplitude of residual dipoles in our maps, after foreground removal (Sect. 5.1). From 100 to 217 GHz, both methods show consistency with WMAP at better than 0.3%. The second approach shows agreement at 1% for 353 GHz. As the data are calibrated on the WMAP dipole measurement, an additional uncertainty of 0.24% has to be combined with the HFI intrinsic uncertainties. Due to the nature of the calibrator, the absolute accuracies stated here only apply at very low ℓ. When studying smaller angular scale anisotropies, transfer functions, including that resulting from the – yet unaccounted for – very long time constants (see Sect. 3.1), should be taken into account.
Indeed the comparison of HFI with WMAP C_ℓ measurements at the level of the first and second peak show a discrepancy of 2.4% in spectra, thus a possible calibration discrepancy of 1.2% (Planck Collaboration XVI 2014). Considering the relative calibration accuracy discussed above this must come from a common systematic effect on either the HFI CMB channels or on the WMAP V and W data, affecting the dipole calibrations and/or the transfer functions.
For the two highest frequencies, the absolute scale is limited by the accuracy of the planetary atmosphere models (5%), combined with systematic uncertainties in our flux measurements (5%), which results in a total uncertainty of 10%. Such uncertainties are relevant for comparing *Planck* data with

Table 11. Summary of the HFI systematic calibration uncertainties for the frequency maps of the 2013 data release.

Frequency [GHz]	Time stability (a) [%]	Relative (b) [%]	Absolute (c) [%]	Model [%]
100	0.3	0.2	0.54	0.24
143	0.3	0.2	0.54	0.24
217	0.3	0.2	0.54	0.24
353	1.0	1.0	1.24	0.24
545	1.0	5.0	10.0	5.0
857	1.0	5.0	10.0	5.0

Notes. Column (a) gives the residual relative variation of calibration with time, (b) gives the relative calibration uncertainty from one HFI channel to the other, and (c) the absolute calibration uncertainties of each HFI channel, including the uncertainties of the calibrators (WMAP dipole and models of planets) that are listed in the last column. These have to be taken into account when comparing with data sets relying on the same calibrators.

other data sets. When comparing with data sets sharing the same calibrator as HFI, the WMAP dipole or the planet models of Moreno (2010), the uncertainty on these calibrators should therefore be omitted in the comparison.

We summarize the calibration uncertainties for the HFI frequency maps in Table 11.

Acknowledgements. The development of *Planck* has been supported by: ESA; CNES and CNRS/INSU-IN2P3-INP (France); ASI, CNR, and INAF (Italy); NASA and DoE (USA); STFC and UKSA (UK); CSIC, MICINN and JA (Spain); Tekes, AoF and CSC (Finland); DLR and MPG (Germany); CSA (Canada); DTU Space (Denmark); SER/SSO (Switzerland); RCN (Norway); SFI (Ireland); FCT/MCTES (Portugal); and PRACE (EU). A description of the *Planck* Collaboration and a list of its members with the technical or scientific activities they have been involved into, can be found at http://www.rssd.esa.int/index.php?project=PLANCK&page=PlanckCollaboration

Appendix A: Calibration conventions

A.1. Colour corrections

Whatever the origin of the calibrator (on the sky or with an internal blackbody), the calibration is performed with a source of known spectral energy distribution (SED). Except for CMB anisotropies, in general, the observed source will have a SED different from the calibration source. Although the simplest way to express the calibration is to give the response as a function of the power falling onto the detector, we usually use a secondary expression of the measurements as spectral densities. This allows us to compare the measurements with other experiments, and with models. Spectral densities are either an intensity (W m^{-2} sr^{-1} Hz^{-1}) for brightness or flux densities (W m^{-2} Hz^{-1}) for unresolved sources, expressed at a reference frequency such that the power integrated in the spectral bandpass is equal to the measured power. The intensity (or flux density) is thus always linked to the choice of both a reference frequency and an assumed SED.

CMB anisotropies are calibrated on the CMB dipoles (and inter-calibrated on higher-order CMB anisotropies). The CMB temperature gives a calibration only for the SED of the CMB anisotropies. CMB anisotropies are thus expressed as δT in K_{CMB}. For astrophysical components with a different SED, this calibration has to be re-expressed as an intensity at the reference frequency, using a SED convention. Following the *IRAS* convention, the spectral intensity data I_ν, are often expressed at fixed nominal frequencies, assuming the source spectrum is νI_ν = constant (i.e., constant intensity per logarithmic frequency interval, labelled "ref"). The colour correction factor C is defined such that:

$$I_{\nu_0}^{\rm act} = \frac{I_{\nu_0}^{\rm ref}}{C}, \tag{A.1}$$

where $I_{\nu_0}^{\rm act}$ is the actual specific intensity of the sky at frequency ν_0, $I_{\nu_0}^{\rm ref}$ is the corresponding value given with the *IRAS* (Neugebauer et al. 1984) or DIRBE (Silverberg et al. 1993) convention[6] and ν_0 is the frequency corresponding to the nominal wavelength of the band. With these definitions,

$$C = \frac{\int (I_\nu/I_{\nu_0})^{\rm act} R_\nu {\rm d}\nu}{\int (\nu_0/\nu) R_\nu {\rm d}\nu}, \tag{A.2}$$

where $(I_\nu/I_{\nu_0})_{\rm act}$ is the actual specific intensity of the sky normalized to the intensity at frequency ν_0, and R_ν is the spectral response (see Planck Collaboration IX 2014).

A.2. CMB dipole conventions

Unlike the LFI calibration (Planck Collaboration V 2014), we used the non-relativistic approximation of the dipole anisotropy for HFI calibration at low frequency:

$$\frac{\delta T}{T} = \beta \cos\theta, \tag{A.3}$$

where $\beta = v/c$ is the ratio between the observer velocity v and the speed of light. For the CMB dipole, $\beta \simeq 1.2 \times 10^{-3}$. The leading-order term of the relativistic corrections is $\beta^2(\cos^2\theta - 1/2)$ (Peebles & Wilkinson 1968; Kamionkowski & Knox 2003; Planck Collaboration XXVII 2014). The amplitude of this correction is of $\pm 1/2\beta^2$, so this quadrupole term has a relative amplitude of 0.6×10^{-3} with respect to the non-relativistic term of Eq. (A.3). However, this quadrupole is only coupled to the dipole when masking part of the sky, which is small (~10%) in our calibration scheme, so the real bias must be smaller. Indeed, when using the orbital dipole as the calibrator, which is a factor of about 10 smaller than the solar dipole, Tristram et al. (2011) showed that using the non-relativistic approximation leads to a relative bias as small as 6×10^{-6}. Given the level of systematic uncertainties we estimate for our calibration, it is therefore legitimate, and much simpler, to use the non-relativistic approximation of the solar dipole anisotropy.

A.3. Far sidelobes

The impact of far sidelobes (FSL) on HFI data is discussed in detail in Planck Collaboration VII (2014). We present only a summary of their impact for the calibration in this appendix.

FSL may affect the calibration determination in different ways. The power measured by our detectors $p_{\rm mes}$ may be schematically written as:

$$p_{\rm mes} = g(S_{\rm ML} + S_{\rm FSL}) + {\rm noise} \tag{A.4}$$

where $S_{\rm ML}$ denotes the sky signal coming through the main lobe and $S_{\rm FSL}$ that coming through the far sidelobes. We also denote by $f_{\rm FSL}$ the fraction of power going into the FSL. For the planet photometry, some level of knowledge of $f_{\rm FSL}$ is needed to correctly compare the reconstructed flux with the planet brightness.

[6] The DIRBE and IRAS data products give $I_{\nu_0}(\nu I_\nu$ = constant).

However, the relative FSL power is lower than 0.3% (Tauber et al. 2010) for all HFI frequencies, which is well below the systematic uncertainties in the planet emission models that we are using, which are about 5% (see Sect. 4). Therefore FSL can safely be ignored in the 545 and 857 GHz calibration analyses.

For the diffuse emission calibration on the CMB dipole at low HFI frequencies, we use a fit of the observed data to the solar dipole as measured by the WMAP team (Hinshaw et al. 2009) (see Sect. 3), without convolving it with a beam model. Note that this is different from the LFI calibration pipeline (Planck Collaboration V 2014). To clarify the consequences of this choice, we have to examine the FSL signal in detail. The FSL signal may be decomposed to first order into three main components, depending on their optical paths: the primary, named PR, and the secondary and baffle spillovers collectively named SR in Tauber et al. (2010). The primary spillover originates mainly from directions on the sky close to the spin axis, so is will be roughly constant for each fixed pointing period and will be removed by our destriping procedure. The baffle spillover corresponds to radiation reaching the detectors after reflection on material surrounding the mirrors, including the telescope's baffles. Again, one may expect this component to be roughly constant over a ring, as a result of the averaging of many original directions. Finally, the secondary spillover comes from a wide ($\sim 15^\circ \times 30^\circ$) area centered about 10° away from the main beam (see Fig. 5 in Tauber et al. 2010). It is formed by radiation reaching the HFI horns without any reflection on telescope parts. It generates an image of the sky offset with respect to the main beam, and integrated over a very broad area. In particular, it contains a dipole component.

Table 2 in Tauber et al. (2010) gives the relative amplitudes of the different FSL components with respect to the main beam signal, combining the secondary and baffle spillovers in the "SR" column. One may see that PR and SR have comparable amplitudes. At maximum, the SR relative amplitude amounts to 0.2% at 100 GHz and decreases fast for frequencies higher that 217 GHz. To clarify the importance of the baffle spillovers, we performed simulations with the actual *Planck* scanning strategy and FSL models similar to those of Tauber et al. (2010). The simulations show that the SR FSL signal after destriping has an amplitude of about 70% of the value listed in Table 2 of Tauber et al. (2010). This is confirmed by the estimate of the FSL amplitudes presented in Planck Collaboration XIV (2014), which gives confidence in the models used in Tauber et al. (2010). From this analysis, and as shown in Planck Collaboration VII (2014), we conclude that, at maximum, a spurious dipolar signal with a relative amplitude of ~0.13% could be present in our data. As the CMB is a Gaussian signal, neglecting the beam transfer function, i.e., at very low ℓ ($\ell \leq 30$ given the SR beam), one may then consider that

$$S_{\rm FSL} = \varepsilon_{\rm SR} S_{\rm ML} + \text{constant} \qquad \text{(A.5)}$$

at ring level. Thus our calibration will determine an effective gain: $g_{\rm eff} = g(1 + \varepsilon_{\rm SR})$. This will lead at these scales to a reconstructed sky signal approximately equal to $S_{\rm ML}$. Therefore, at large angular scales, if we ignore the spurious SR signal remaining after destriping in the calibration process, this gain overestimation cancels to first order the effect of not accounting for the SR part in further analysis (like power spectra). At smaller scales, however, the SR signal becomes negligible and this cancellation is not effective anymore. To summarize, the HFI dipole calibration as performed for the 2013 data release may result in an approximately 0.25% overestimate of the band powers for ℓ above about 40. This calibration systematic effect (roughly 0.13%) is lower than other sources of systematic uncertainties evaluated in this paper.

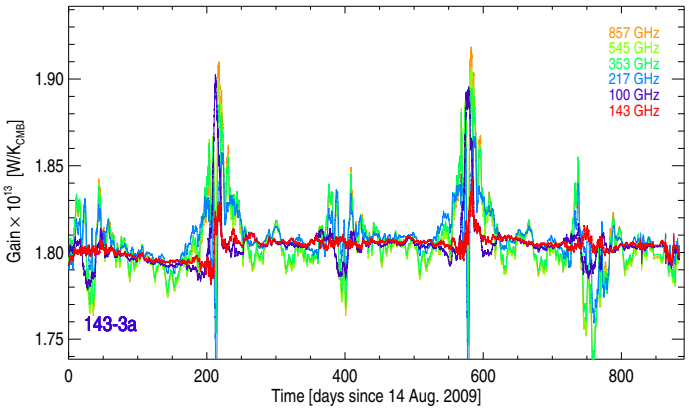

Fig. B.1. Impact of the Galactic template on the solar dipole ring-gain measurements, for one detector at 143 GHz. We compare the results obtained using the HFI temperature maps at each frequency (from, e.g., previous reconstructions). For this plot, ring-by-ring gains have been smoothed with a width of 50 rings (which corresponds to about 2 days). The largest variations occur for rings for which the solar dipole amplitude is low relative to the Galactic emission (around days 50, 200, 400, 550, and 700). Using the HFI map at the detector's frequency as a Galactic template minimizes the systematic ring-to-ring variations.

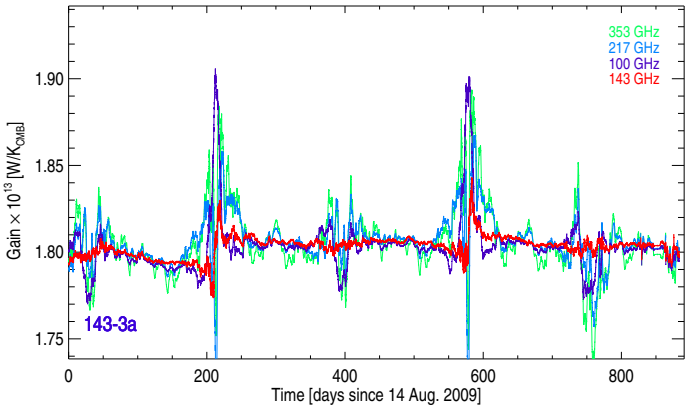

Fig. B.2. Same as Fig. B.1, but taking into account polarization as reconstructed in the HFI Q and U maps. This makes very little difference in the results, showing that polarization is not the main source of systematic variations for the rings where the Galactic emission is large.

Appendix B: Choosing the sky template for the solar dipole calibration

To determine the solar dipole calibration factor, we have to take into account the Galactic foreground. This is done with a template (see Sect. 3.2). Figure B.1 shows the impact of the choice of Galactic template. We compare the ring-by-ring gains obtained with each of the HFI frequency maps. Using a Galactic template helps improve the estimation of the calibration factor for rings scanning regions close to the Galactic equator (e.g., around day 200). Unsurprisingly, the template producing the lowest apparent variations is that with the same frequency as the detector of interest. However, even in this case, apparent systematic gain variations are observed at the times when the dipole amplitude is low, In Fig. B.2 we show results obtained taking into account the polarization (from the HFI Q and U maps). The small difference this induces shows that polarization does not

play a major role in the apparent ring-to-ring variations, even for rings where Galactic emission is larger.

Appendix C: HFI and FIRAS data comparison

The procedure we used to compare HFI and FIRAS data is very similar to that adopted by the ARCHEOPS collaboration (Macías-Pérez et al. 2007). It has been summarized in Planck HFI Core Team (2011b) and we give here the full details.

C.1. FIRAS data: spectra and derived maps

FIRAS spectra The FIRAS instrument, its operating modes, calibration, and the data products are described in the FIRAS Explanatory Supplement (FIRAS team 1997, http://lambda.gsfc.nasa.gov/product/cobe/firas_exsupv4.cfm). FIRAS has a scanning, four-port (two inputs; two outputs) Michelson interferometer that uses polarizing grids as beam-splitters and creates an interferogram (i.e., the Fourier transform of the source spectrum) by scanning a movable mirror platform (the "Mirror Transport Mechanism", or MTM). A dichroic splitter at each output port (designated "left" or "right") further splits each beam into low (30–630 GHz) and high (600–2910 GHz) frequency bands. The MTM could be scanned at either of two speeds: "slow" or "fast". Furthermore the MTM sweep could be set to one of two scan lengths, "long" or "short", thus affecting the spectral resolution. Most research applications call for one or more high-level products, such as the dust spectrum maps that we are using here. In these high-level products, the different modes and detector signals were combined to form the HIGH and LOWF frequency data-sets. The two dust-spectrum maps (FIRAS_DUST_SPECTRUM_HIGH.FITS and FIRAS_DUST_SPECTRUM_LOWF.FITS) cover 98.7% of the sky and give the residual sky spectrum, from about 2970 to 68 GHz, after modelled emission from the CMB, interplanetary dust, and interstellar lines has been subtracted. The remaining signal is thus dominated by thermal continuum emission from Galactic interstellar dust (and the cosmic IR background e.g., Puget et al. 1996; Fixsen et al. 1998 and Lagache et al. 1999).

Uncertainty estimates. Uncertainties in the FIRAS data are fully detailed in the FIRAS explanatory supplement. The errors are divided into several groups: the detector measurements; the calibration emissivities; the bolometer model parameters; the temperature measurements of all but XCAL (XCAL is the external Calibrator); and the temperature measurement of the XCAL. For our purposes, only the detector noise, the uncertainties in some parameters derived from the calibration, and the uncertainty in the absolute temperature scale of the external calibrator are of importance. The covariance matrix can be written as:

$$\mathbf{V} = \mathbf{C} + \mathbf{J} + \mathbf{P}. \tag{C.1}$$

The **C** term (called the **C**-matrix by the FIRAS team) is the detector noise. It includes off-diagonal terms due to frequency correlations introduced by the smoothing of the coadded interferograms, before Fourier transformation into spectra. The **J** term (called JCJ by the FIRAS team) corresponds to uncertainties linked to the bolometer model parameters (only the JCJ gain is important here). This error has to be considered as a systematic error. The **P** term (called PTP by the FIRAS team) is the absolute thermometry uncertainty; it is not a statistical uncertainty. It is included in the error budget since it is the dominant error for the absolute temperature of the CMB. It is thus important for comparison of FIRAS measurements to other experiments (but only for frequencies smaller than about 430 GHz). The levels of these three uncertainties are shown in Fig. C.1. For the detector noise, only the square root of the diagonal (the "$\boldsymbol{C}$-vector") is displayed. Fixsen et al. (1997) used a conservative estimate of the gain uncertainty of 2% for the 600−2400 GHz FIRAS data.

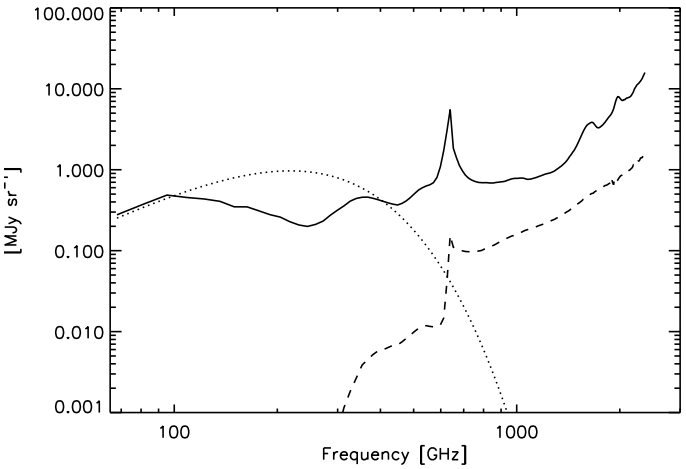

Fig. C.1. FIRAS uncertainty summary. Only the uncertainties relevant for our purpose are displayed here: the $\boldsymbol{C}$-vector (continuous line), the JCJ gain multiplied by the average sky spectrum (dashed line), and the PTP uncertainty (dotted line).

Building FIRAS maps FIRAS maps at the Planck frequency can be obtained by convolving the FIRAS spectra with the *Planck*-HFI bandpass filters. However, this method gives very noisy FIRAS maps (especially for $\nu < 430$ GHz). Thus, we derived FIRAS maps together with their errors from fits of FIRAS spectra. Each individual spectrum is fitted with a modified blackbody spectrum,

$$S_\nu = \tau \left(\frac{\nu}{\nu_0}\right)^\beta P(\nu, T_{\rm dust}), \tag{C.2}$$

where τ is a measure of the relative dust column density for each pixel, β is the spectral index, and $P(\nu, T_{\rm dust})$ is the blackbody function. Since we are searching for the best representation of the data and not for physical dust parameters, we include the contribution of the cosmic infrared background in the fit. Moreover, we restrict the fit to the frequency range of interest – this avoids the need for a second dust component as in Finkbeiner et al. (1999).

For all HFI frequencies, we find the best values of τ, $T_{\rm dust}$, and β for each FIRAS pixel using a χ^2 minimization. We include the correlations between FIRAS frequencies, and fit in frequency intervals related to the frequency of interest. Only the C-matrix was considered in the fit. The JCJ and PTP terms are added as systematic errors at the end of the process.

Ideally, the fits would have to be performed on independent frequency intervals so that the maps derived for each of the *Planck*-HFI frequencies are independent. However reducing the frequency interval increases the noise, so it was necessary to use overlapping frequency intervals. Fortunately, the fitting results are not very sensitive to the choice of the intervals; there are no systematic effects, and the values derived at the *Planck*-HFI wavelengths are consistent. This is not the case for the error bars, that can vary by factors of 2. Fits are performed for $560 < \nu < 1765$ GHz, $400 < \nu < 1500$ GHz, $270 < \nu < 1000$ GHz,

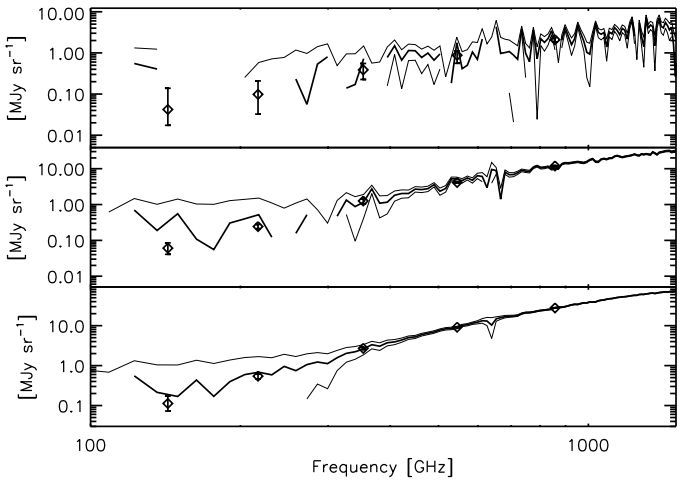

Fig. C.2. Example of FIRAS spectra (with their $\pm 1\sigma$ error) with the derived values at the HFI frequencies.

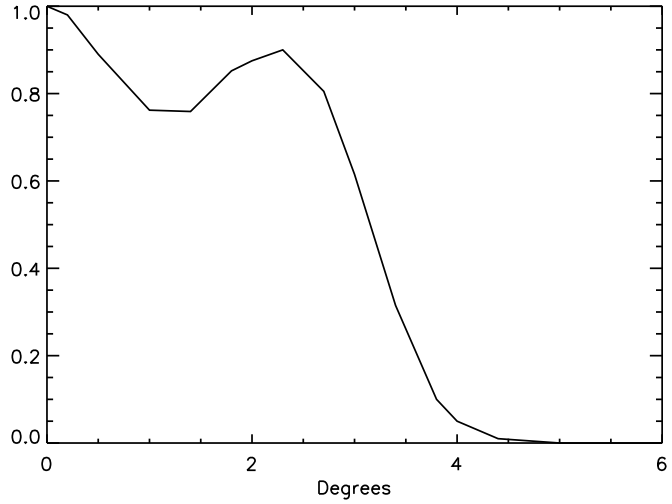

Fig. C.3. FIRAS beam profile (from http://lambda.gsfc.nasa.gov/product/cobe/firas_prod_table.cfm).

$170 < \nu < 860$ GHz and $75 < \nu < 670$ GHz for the 857, 545, 353, 217, and 143 GHz HFI frequencies, respectively. Typically, at Galactic latitudes $|b| < 5°$, 1σ uncertainties are about 1.0, 1.5, 4.2, 9.8, and 35.1% at 857, 545, 353, 217 and 143 GHz, respectively. They reach 5.5, 11, 29, 54, and 158% for $15° < |b| < 20°$. Figure C.2 shows the results for three different pixels.

C.2. *Planck*-HFI data: towards the FIRAS resolution

We construct uncalibrated *Planck* maps for each detector, and convolved them with the FIRAS beam.

FIRAS beam The FIRAS beam has been measured using the Moon. Due to imperfections in the sky horn antenna, the effective beam shows both radial and azimuthal deviations from the nominal 7° top-hat beam profile (Fig. C.3). Since COBE rotates about the optical axis of the FIRAS instrument, the average beam has a circular symmetry; but a single interferogram is acquired in less than a rotation period and thus can have an asymmetric beam. Fixsen et al. (1997) estimate that the assumption of beam symmetry may produce residual beam shape errors of order of 5%, and we take this into account in what follows.

Convolution We carry out the beam convolution in the `HEALPix` scheme. To simulate the movement during the integration of an interferogram, the data were further convolved by a $2\overset{\circ}{.}6$ top-hat in the direction perpendicular to the ecliptic plane (which is roughly the FIRAS scanning direction).

C.3. FIRAS data: towards the `HEALPix` projection

The *Planck* maps are presented in the `HEALPix` format (Górski et al. 2005) with a resolution $N_{\rm side} = 2048$. For comparison with FIRAS, the convolved HFI maps are downgraded to $N_{\rm side} = 32$. COBE data are presented in the COBE Quadrilateralized Spherical Cube projection (CSC), an approximately equal-area projection. For comparison with *Planck*, the FIRAS maps are re-gridded into the `HEALPix` format, using a drizzling re-projection code.

Table C.1. Uncertainties on the zero points (in MJy sr^{-1} [νI_ν = constant]).

Detector	Statistical	Systematic	Sum
857-1	0.23	2.40	2.63
545-1	0.67	0.65	1.32
353-1	0.57	1.78	2.25
217-1	0.57	1.08	1.65
143-5	0.61	0.66	1.27
100-1a	0.85	0.42	1.27

C.4. Deriving the calibration gains and zero points

We fit for the calibration coefficients K and O following:

$$F(\nu_0)/C = K \times H(\nu_0) + O, \tag{C.3}$$

where $F(\nu_0)$ is the FIRAS brightness at frequency ν_0, $H(\nu_0)$ is the HFI signal in pW at ν_0, K is the gain calibration factor (for a source spectrum with νI_ν = constant), and C is the colour correction given in Eq. (A.1). The calibration coefficients K and O are derived from a linear fit of the FIRAS and HFI cosecant variations, restricted to intermediate Galactic latitudes ($10° < |b| < 60°$). We avoid using the inner part of the Galactic plane, as the spectral characteristics, averaged out in the FIRAS measurements, may present angular scale variations that are not accurately accounted for in our processing of the HFI data (i.e., we evaluate K and C at 7° resolution, not 5′). More importantly, we avoid the inner part to minimize the effect of the FIRAS beam uncertainties. The Galactic polar caps are also not used, since the signal-to-noise ratio of the FIRAS data extrapolation is very low there. We also mask regions where CO emission lines (removed from FIRAS measured spectra) are bright in the Dame et al. (1987) map, and add a template of CMB anisotropies to the FIRAS data.

We use Eq. (C.3) to fit for both the gain and offset for each HFI detector, and use the measured offset to compute the zero level of HFI maps. Statistical errors are dominated by the FIRAS errors (the HFI errors are negligible). The error on O is dominated by the systematic effect observed on the gain K (see next section). We use the dispersion of the values obtained in different parts of the sky as an estimate of the systematic error. This error is about 3% at 857, 5% at 545, 5% at 353, and 10% at 143 GHz.

Table C.2. CIB mean values computed in some extragalactic fields (N1, SP, AG, LH, and Bootes, see Planck Collaboration XVIII (2011) for more details), and expected from Lagache et al. (1999) FIRAS measurements, and from the Béthermin et al. (2012) model (also given in Table 4).

Frequency [GHz]	CIB from HFI [MJy sr^{-1}] (νI_ν = constant)	CIB measured from FIRAS [MJy sr^{-1}] (νI_ν = constant)	CIB from Béthermin et al. (2012) [MJy sr^{-1}] (νI_ν = constant)
857	0.29	0.71 ± 0.23	0.64
545	0.18	0.37 ± 0.12	0.35
353	0.09	0.13 ± 0.04	0.13
217	2.2×10^{-2}	$(3.4 \pm 1.1) \times 10^{-2}$	3.3×10^{-2}

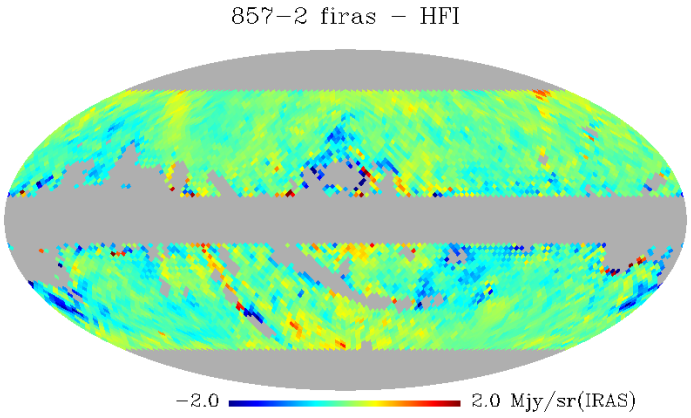

Fig. C.4. FIRAS minus convolved-HFI data for the 857-2 detector (in MJy sr^{-1}). Only pixels used for the "nominal" calibration are shown (i.e., $10° < |b| < 60°$, outside the CO mask, and for pixels with enough FIRAS coverage)

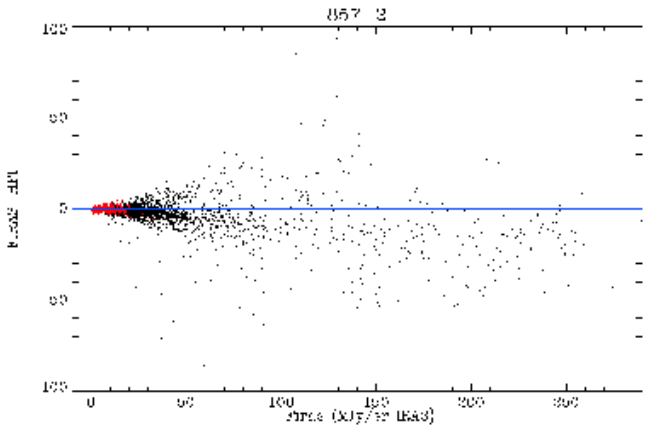

Fig. C.5. Scatter plot of FIRAS minus convolved-HFI versus FIRAS (in MJy sr^{-1}). On average, the difference becomes more negative as the brightness increases. The red points are those used to compute the nominal calibration coefficients. HFI is clearly overestimated relative to FIRAS at high brightness.

At 217 and 100 GHz, since we have no way to address the variations on the sky without removing the CO contamination, we also take 10% as the systematic error. For the total error on O, we sum the statistical and systematic errors linearly. Errors for some individual bolometers are given in Table C.1.

Using the frequency maps and the dedicated component separation done in the CIB fields by (Planck Collaboration XVIII 2011), we can compute the CIB mean value in those fields and compare them with the expected values (see Table C.2). Although the error bars on the measured CIB at low frequencies are quite large, we see a systematic trend: the measured CIB is systematically lower than the expected CIB by factors of 2.4, 2, 1.4, and 1.5 at 857, 545, 353, and 217 GHz, respectively.

An example of a residual map is shown in Fig. C.4. We see that in the sky area used to compute the calibration coefficients the residual is close to zero, except for nearby bright regions (e.g., the Taurus cloud), where the FIRAS brightness is underestimated compared to HFI.

C.5. Systematic effects in the calibration coefficients

As already mentioned, we observe spatial variations of the FIRAS calibration gain (i.e., a variation of K, and thus of O). Indeed, the calibration coefficients recovered from the narrow part of the Galactic plane differ by 10−15% from the coefficients derived at intermediate Galactic latitude (see Fig. C.5). To understand this discrepancy, we consulted the FIRAS team on: (1) the FIRAS beam knowledge and its potential changes with frequency, with the FIRAS beam to first order being independent of frequency (given by a geometrical optics dominated horn); and (2) non-linearity effects. None of these can explain the discrepancy. We also investigated several other possibilities:

- Pixelization: FIRAS data and errors are given in the quadrilateralized spherical cube projection[7]. In the nominal pipeline, we computed the calibration gain K after reprojecting FIRAS data onto the `HEALPix` grid. We also reprojected the HFI data onto the cube (using several schemes for the pixel decimation) to compare the HFI and FIRAS data. We find no difference in the photometric calibration.
- FIRAS beam: beam uncertainty could result in some variations of K where the signal is rapidly varying on the sky (Galactic plane, molecular clouds, bright cirrus regions). In the HFI calibration, we do not account for FIRAS beam variations with frequency. But we tested several "beam configurations" to investigate their impact on the calibration. First, we measured the beam window function B_ℓ using full-sky FIRAS and HFI power spectra. A good fit is obtained for a Gaussian with a $FWHM = 4.^\circ94$. We used this beam in the convolution rather than the "nominal beam" to cross-calibrate the two data sets. We also used other FWHMs (4°, 8°, and 10°). We could not find any beam that reconciles the FIRAS and HFI data.
- Colour corrections: To compute K we need to correct the data for the variation of the spectral energy distribution of dust emission across the sky. Working at 7° and having the FIRAS dust spectrum for each pixel, it was easier to compute the colour correction at the FIRAS resolution ($C[7°]$). However,

$$C[7°] \int_{7°} S_\nu[5']\mathrm{d}\Omega \neq \int_{7°} C[5']S_\nu[5']\mathrm{d}\Omega, \quad \text{(C.4)}$$

[7] FIRAS data in `HEALPix` format are available in NASA's Legacy Archive for Microwave Background Data (`http://lambda.gsfc.nasa.gov`) but the covariance matrix is not provided.

so we checked (for several bolometers) whether the colour corrections could produce the observed spatial variations of K. For that purpose, we used the *Planck* DR2 all-sky temperature map obtained by fitting HFI and IRAS data with a spectral index equal to 1.8 (see Planck Collaboration XIX 2011), to compute a colour-correction map for each HFI pixel, and we modified the calibration pipeline to use this $C[5']$. A strong variation of K was still observed, comparable to the variation observed using $C[7^\circ]$. These refined colour corrections cannot explain the variation of K across the sky. Note however, that using $C[5']$ rather than $C[7^\circ]$ significantly changes the calibration coefficient for the 545 GHz channels, by 6% (although it does not change the 857 GHz coefficients).
- Zodiacal light: The FIRAS data set we are using has the zodiacal emission removed using the COBE model. When comparing HFI and FIRAS data, zodiacal residuals are clearly visible in the difference map. We therefore redid the photometric calibration using the HFI data with the zodiacal light removed. The difference [FIRAS $- K \times$ HFI] does not show any zodiacal residuals. Removing the zodiacal emission decreases the calibration coefficient by less than 2% at 857 GHz but it does not decrease the observed spatial variations of K.
- Far sidelobes: we tested whether far sidelobes could have any impact on the photometric calibration, by looking at the detectors that have very low far-sidelobe contamination (e.g., 857-2). We noticed that the spatial variation of K is of the same order, whatever the FSL contamination.
- Time gain variations: we have searched, unsuccessfully, for any temporal gain variations by calibrating independently each HFI all-sky survey maps.

We thus have no explanation for this effect other than a possible systematic bias in the FIRAS `pass4` interstellar dust spectra.

If the HFI brightness is calibrated using FIRAS, several results suggest that the HFI brightness is overestimated for the high-frequency channels:

- The SEDs of point sources and diffuse dust show an excess at 545 GHz over a smooth interpolation between higher and lower frequencies. A simple interpolation between 857 and 353 GHz shows that the excess is about 11%. Using a very simple dust model, a residual dipole is also present in the 545 GHz maps.
- The CMB anisotropy power spectrum is detectable at 545 GHz and the `SMICA` component separation method shows a (20.3 ± 4.7)% calibration discrepancy. The analysis of the FFP6 simulated data sets shows that the same method gives reliable results at all HFI frequencies.
- The dipole calibration at 545 GHz, although quite uncertain, is also discrepant by about 20% with the FIRAS calibration.
- The measurements on planets (Mars, Jupiter, Saturn, Uranus, and Neptune) used for beam determination and pointing are higher than the models for the two sub-millimetre channels, at least for the detectors that are not affected by non-linearity effects.

We therefore abandoned the FIRAS calibration and used the planet calibration instead.

References

Ashdown, M. A. J., Baccigalupi, C., Bartlett, J. G., et al. 2009, A&A, 493, 753
Béthermin, M., Daddi, E., Magdis, G., et al. 2012, ApJ, 757, L23
Cardoso, J., Martin, M., Delabrouille, J., Betoule, M., & Patanchon, G. 2008, IEEE J. Select. Topics in Signal Process., 2, 735
Dame, T. M., Ungerechts, H., Cohen, R. S., et al. 1987, ApJ, 322, 706
Finkbeiner, D. P., Davis, M., & Schlegel, D. J. 1999, ApJ, 524, 867
Fixsen, D. J., Weiland, J. L., Brodd, S., et al. 1997, ApJ, 490, 482
Fixsen, D. J., Dwek, E., Mather, J. C., Bennett, C. L., & Shafer, R. A. 1998, ApJ, 508, 123
Gispert, R., Lagache, G., & Puget, J. L. 2000, A&A, 360, 1
Górski, K. M., Hivon, E., Banday, A. J., et al. 2005, ApJ, 622, 759
Griffin, M. J., Abergel, A., Abreu, A., et al. 2010, A&A, 518, L3
Hinshaw, G., Weiland, J. L., Hill, R. S., et al. 2009, ApJS, 180, 225
Kalberla, P. M. W., Burton, W. B., Hartmann, D., et al. 2005, A&A, 440, 775
Kamionkowski, M., & Knox, L. 2003, Phys. Rev. D, 67, 3001
Lagache, G., Abergel, A., Boulanger, F., Désert, F. X., & Puget, J.-L. 1999, A&A, 344, 322
Liang, Z., Fixsen, D. J., & Gold, B. 2012, MNRAS, submitted [arXiv:1201.0060]
Lindal, G. F. 1992, AJ, 103, 967
Macías-Pérez, J. F., Lagache, G., Maffei, B., et al. 2007, A&A, 467, 1313
Maffei, B., Noviello, F., Murphy, J. A., et al. 2010, A&A, 520, A12
Mather, J. C., Fixsen, D. J., Shafer, R. A., Mosier, C., & Wilkinson, D. T. 1999, ApJ, 512, 511
Molinari, S., Swinyard, B., Bally, J., et al. 2010, PASP, 122, 314
Moreno, R. 2010, Neptune and Uranus planetary brightness temperature tabulation. Tech. rep., ESA Herschel Science Center, available from ftp://ftp.sciops.esa.int/pub/hsc-calibration/PlanetaryModels/ESA2
Moreno, R., Lellouch, E., Lara, L. M., et al. 2011, A&A, 536, L12
Murphy, J. A., Peacocke, T., Maffei, B., et al. 2010, J. Instrum., 5, 4001
Neugebauer, G., Habing, H. J., van Duinen, R., et al. 1984, ApJ, 278, L1
Peebles, P. J. E., & Wilkinson, D. T. 1968, Phys. Rev., 174, 2168
Perdereau, O. 2006, in CMB and Physics of the Early Universe
Planck Collaboration II. 2011, A&A, 536, A2
Planck Collaboration XVIII. 2011, A&A, 536, A18
Planck Collaboration XIX. 2011, A&A, 536, A19
Planck Collaboration XXIV. 2011, A&A, 536, A24
Planck Collaboration I. 2014, A&A, 571, A1
Planck Collaboration II. 2014, A&A, 571, A2
Planck Collaboration III. 2014, A&A, 571, A3
Planck Collaboration IV. 2014, A&A, 571, A4
Planck Collaboration V. 2014, A&A, 571, A5
Planck Collaboration VI. 2014, A&A, 571, A6
Planck Collaboration VII. 2014, A&A, 571, A7
Planck Collaboration VIII. 2014, A&A, 571, A8
Planck Collaboration IX. 2014, A&A, 571, A9
Planck Collaboration X. 2014, A&A, 571, A10
Planck Collaboration XI. 2014, A&A, 571, A11
Planck Collaboration XII. 2014, A&A, 571, A12
Planck Collaboration XIII. 2014, A&A, 571, A13
Planck Collaboration XIV. 2014, A&A, 571, A14
Planck Collaboration XV. 2014, A&A, 571, A15
Planck Collaboration XVI. 2014, A&A, 571, A16
Planck Collaboration XVII. 2014, A&A, 571, A17
Planck Collaboration XVIII. 2014, A&A, 571, A18
Planck Collaboration XIX. 2014, A&A, 571, A19
Planck Collaboration XX. 2014, A&A, 571, A20
Planck Collaboration XXI. 2014, A&A, 571, A21
Planck Collaboration XXII. 2014, A&A, 571, A22
Planck Collaboration XXIII. 2014, A&A, 571, A23
Planck Collaboration XXIV. 2014, A&A, 571, A24
Planck Collaboration XXV. 2014, A&A, 571, A25
Planck Collaboration XXVI. 2014, A&A, 571, A26
Planck Collaboration XXVII. 2014, A&A, 571, A27
Planck Collaboration XXVIII. 2014, A&A, 571, A28
Planck Collaboration XXIX. 2014, A&A, 571, A29
Planck Collaboration XXX. 2014, A&A, 571, A30
Planck Collaboration XXXI. 2014, A&A, 571, A31
Planck HFI Core Team 2011a, A&A, 536, A4
Planck HFI Core Team 2011b, A&A, 536, A6
Puget, J.-L., Abergel, A., Bernard, J.-P., et al. 1996, A&A, 308, L5
Silverberg, R. F., Hauser, M. G., Boggess, N. W., et al. 1993, in SPIE Conf. Ser. 2019, ed. M. S. Scholl, 180
Tauber, J. A., Norgaard-Nielsen, H. U., Ade, P. A. R., et al. 2010, A&A, 520, A2
Tristram, M., Macías-Pérez, J. F., Renault, C., & Santos, D. 2005, MNRAS, 358, 833
Tristram, M., Filliard, C., Perdereau, O., et al. 2011, A&A, 534, A88
Yu, Q., Spergel, D. N., & Ostriker, J. P. 2001, ApJ, 558, 23

[1] APC, AstroParticule et Cosmologie, Université Paris Diderot, CNRS/IN2P3, CEA/lrfu, Observatoire de Paris, Sorbonne Paris Cité, 10 rue Alice Domon et Léonie Duquet, 75205 Paris Cedex 13, France
[2] Aalto University Metsähovi Radio Observatory and Dept of Radio Science and Engineering, PO Box 13000, 00076 AALTO, Finland
[3] African Institute for Mathematical Sciences, 6-8 Melrose Road, Muizenberg, Cape Town, 7701 Rondebosh, South Africa
[4] Agenzia Spaziale Italiana Science Data Center, via del Politecnico snc, 00133 Roma, Italy
[5] Agenzia Spaziale Italiana, Viale Liegi 26, 00498 Roma, Italy
[6] Astrophysics Group, Cavendish Laboratory, University of Cambridge, J J Thomson Avenue, Cambridge CB3 0HE, UK
[7] Astrophysics & Cosmology Research Unit, School of Mathematics, Statistics & Computer Science, University of KwaZulu-Natal, Westville Campus, Private Bag X54001, 4000 Durban, South Africa
[8] Atacama Large Millimeter/submillimeter Array, ALMA Santiago Central Offices, Alonso de Cordova 3107, Vitacura, Casilla 763 0355 Santiago, Chile
[9] CITA, University of Toronto, 60 St. George St., Toronto, ON M5S 3H8, Canada
[10] CNRS, IRAP, 9 Av. colonel Roche, BP 44346, 31028 Toulouse Cedex 4, France
[11] California Institute of Technology, Pasadena, California, USA
[12] Centre for Theoretical Cosmology, DAMTP, University of Cambridge, Wilberforce Road, Cambridge CB3 0WA, UK
[13] Centro de Estudios de Física del Cosmos de Aragón (CEFCA), Plaza San Juan, 1, planta 2, 44001 Teruel, Spain
[14] Computational Cosmology Center, Lawrence Berkeley National Laboratory, Berkeley, California, USA
[15] DSM/Irfu/SPP, CEA-Saclay, 91191 Gif-sur-Yvette Cedex, France
[16] DTU Space, National Space Institute, Technical University of Denmark, Elektrovej 327, 2800 Kgs. Lyngby, Denmark
[17] Département de Physique Théorique, Université de Genève, 24 quai E. Ansermet,1211 Genève 4, Switzerland
[18] Departamento de Física Fundamental, Facultad de Ciencias, Universidad de Salamanca, 37008 Salamanca, Spain
[19] Department of Astronomy and Astrophysics, University of Toronto, 50 Saint George Street, Toronto, Ontario, Canada
[20] Department of Astrophysics/IMAPP, Radboud University Nijmegen, PO Box 9010, 6500 GL Nijmegen, The Netherlands
[21] Department of Electrical Engineering and Computer Sciences, University of California, Berkeley, California, USA
[22] Department of Physics & Astronomy, University of British Columbia, 6224 Agricultural Road, Vancouver, British Columbia, Canada
[23] Department of Physics and Astronomy, Dana and David Dornsife College of Letter, Arts and Sciences, University of Southern California, Los Angeles, CA 90089, USA
[24] Department of Physics and Astronomy, University College London, London WC1E 6BT, UK
[25] Department of Physics, Florida State University, Keen Physics Building, 77 Chieftan Way, Tallahassee, Florida, USA
[26] Department of Physics, Gustaf Hällströmin katu 2a, University of Helsinki, 00014 Helsinki, Finland
[27] Department of Physics, Princeton University, Princeton, New Jersey, USA
[28] Department of Physics, University of California, One Shields Avenue, Davis, California, USA
[29] Department of Physics, University of California, Santa Barbara, California, USA
[30] Department of Physics, University of Illinois at Urbana-Champaign, 1110 West Green Street, Urbana, Illinois, USA
[31] Dipartimento di Fisica e Astronomia G. Galilei, Università degli Studi di Padova, via Marzolo 8, 35131 Padova, Italy
[32] Dipartimento di Fisica e Scienze della Terra, Università di Ferrara, via Saragat 1, 44122 Ferrara, Italy
[33] Dipartimento di Fisica, Università La Sapienza, P.le A. Moro 2, 00185 Roma, Italy
[34] Dipartimento di Fisica, Università degli Studi di Milano, via Celoria 16, 20133 Milano, Italy
[35] Dipartimento di Fisica, Università degli Studi di Trieste, via A. Valerio 2, 34127 Trieste, Italy
[36] Dipartimento di Fisica, Università di Roma Tor Vergata, via della Ricerca Scientifica, 1, 00133 Roma, Italy
[37] Discovery Center, Niels Bohr Institute, Blegdamsvej 17, 2100 Copenhagen, Denmark
[38] European Southern Observatory, ESO Vitacura, Alonso de Cordova 3107, Vitacura, Casilla 19001 Santiago, Chile
[39] European Space Agency, ESAC, Planck Science Office, Camino bajo del Castillo, s/n, Urbanización Villafranca del Castillo, Villanueva de la Cañada, Madrid, Spain
[40] European Space Agency, ESTEC, Keplerlaan 1, 2201 AZ Noordwijk, The Netherlands
[41] Haverford College Astronomy Department, 370 Lancaster Avenue, Haverford, Pennsylvania, USA
[42] Helsinki Institute of Physics, Gustaf Hällströmin katu 2, University of Helsinki, 00014 Helsinki, Finland
[43] INAF − Osservatorio Astrofisico di Catania, via S. Sofia 78, 95123 Catania, Italy
[44] INAF − Osservatorio Astronomico di Padova, Vicolo dell'Osservatorio 5, 35122 Padova, Italy
[45] INAF − Osservatorio Astronomico di Roma, via di Frascati 33, 00044 Monte Porzio Catone, Italy
[46] INAF − Osservatorio Astronomico di Trieste, via G.B. Tiepolo 11, 34131 Trieste, Italy
[47] INAF Istituto di Radioastronomia, via P. Gobetti 101, 40129 Bologna, Italy
[48] INAF/IASF Bologna, via Gobetti 101, 40129 Bologna, Italy
[49] INAF/IASF Milano, via E. Bassini 15, 20133 Milano, Italy
[50] INFN, Sezione di Bologna, via Irnerio 46, 40126, Bologna, Italy
[51] INFN, Sezione di Roma 1, Università di Roma Sapienza, P.le Aldo Moro 2, 00185 Roma, Italy
[52] IPAG: Institut de Planétologie et d'Astrophysique de Grenoble, Université Joseph Fourier, Grenoble 1/CNRS-INSU, UMR 5274, 38041 Grenoble, France
[53] IUCAA, Post Bag 4, Ganeshkhind, Pune University Campus, 411 007 Pune, India
[54] Imperial College London, Astrophysics group, Blackett Laboratory, Prince Consort Road, London, SW7 2AZ, UK
[55] Infrared Processing and Analysis Center, California Institute of Technology, Pasadena, CA 91125, USA
[56] Institut Néel, CNRS, Université Joseph Fourier Grenoble I, 25 rue des Martyrs, Grenoble, France
[57] Institut Universitaire de France, 103 bd Saint-Michel, 75005 Paris, France
[58] Institut d'Astrophysique Spatiale, CNRS (UMR 8617) Université Paris-Sud 11, Bâtiment 121, 91405 Orsay, France
[59] Institut d'Astrophysique de Paris, CNRS (UMR 7095), 98bis boulevard Arago, 75014 Paris, France
[60] Institute for Space Sciences, 077125 Bucharest-Magurale, Romania
[61] Institute of Astronomy and Astrophysics, Academia Sinica, 106 Taipei, Taiwan
[62] Institute of Astronomy, University of Cambridge, Madingley Road, Cambridge CB3 0HA, UK
[63] Institute of Theoretical Astrophysics, University of Oslo, Blindern, 0315 Oslo, Norway
[64] Instituto de Física de Cantabria (CSIC-Universidad de Cantabria), Avda. de los Castros s/n, 39005 Santander, Spain
[65] Jet Propulsion Laboratory, California Institute of Technology, 4800 Oak Grove Drive, Pasadena, California, USA
[66] Jodrell Bank Centre for Astrophysics, Alan Turing Building, School of Physics and Astronomy, The University of Manchester, Oxford Road, Manchester, M13 9PL, UK
[67] Kavli Institute for Cosmology Cambridge, Madingley Road, Cambridge, CB3 0HA, UK
[68] LAL, Université Paris-Sud, CNRS/IN2P3, 91898 Orsay, France

[69] LERMA, CNRS, Observatoire de Paris, 61 avenue de l'Observatoire, 75014 Paris, France
[70] LESIA, Observatoire de Paris, CNRS, UPMC, Université Paris-Diderot, 5 place J. Janssen, 92195 Meudon, France
[71] Laboratoire AIM, IRFU/Service d'Astrophysique – CEA/DSM – CNRS – Université Paris Diderot, Bât. 709, CEA-Saclay, 91191 Gif-sur-Yvette Cedex, France
[72] Laboratoire Traitement et Communication de l'Information, CNRS (UMR 5141) and Télécom ParisTech, 46 rue Barrault, 75634 Paris Cedex 13, France
[73] Laboratoire de Physique Subatomique et de Cosmologie, Université Joseph Fourier Grenoble I, CNRS/IN2P3, Institut National Polytechnique de Grenoble, 53 rue des Martyrs, 38026 Grenoble Cedex, France
[74] Laboratoire de Physique Théorique, Université Paris-Sud 11 & CNRS, Bâtiment 210, 91405 Orsay, France
[75] Lawrence Berkeley National Laboratory, Berkeley, California, USA
[76] Max-Planck-Institut für Astrophysik, Karl-Schwarzschild-Str. 1, 85741 Garching, Germany
[77] McGill Physics, Ernest Rutherford Physics Building, McGill University, 3600 rue University, Montréal, QC, H3A 2T8, Canada
[78] National University of Ireland, Department of Experimental Physics, Maynooth, Co. Kildare, Ireland
[79] Niels Bohr Institute, Blegdamsvej 17, 2100 Copenhagen, Denmark
[80] Observational Cosmology, Mail Stop 367-17, California Institute of Technology, Pasadena, CA 91125, USA
[81] Optical Science Laboratory, University College London, Gower Street, London, UK
[82] SB-ITP-LPPC, EPFL, 1015 Lausanne, Switzerland
[83] SISSA, Astrophysics Sector, via Bonomea 265, 34136 Trieste, Italy
[84] School of Physics and Astronomy, Cardiff University, Queens Buildings, The Parade, Cardiff, CF24 3AA, UK
[85] Space Research Institute (IKI), Russian Academy of Sciences, Profsoyuznaya Str, 84/32, 117997 Moscow, Russia
[86] Space Sciences Laboratory, University of California, Berkeley, California, USA
[87] Special Astrophysical Observatory, Russian Academy of Sciences, Nizhnij Arkhyz, Zelenchukskiy region, 369167 Karachai-Cherkessian Republic, Russia
[88] Stanford University, Dept of Physics, Varian Physics Bldg, 382 via Pueblo Mall, Stanford, California, USA
[89] Sub-Department of Astrophysics, University of Oxford, Keble Road, Oxford OX1 3RH, UK
[90] Theory Division, PH-TH, CERN, 1211 Geneva 23, Switzerland
[91] UPMC Univ Paris 06, UMR7095, 98bis boulevard Arago, 75014 Paris, France
[92] Université de Toulouse, UPS-OMP, IRAP, 31028 Toulouse Cedex 4, France
[93] University of Granada, Departamento de Física Teórica y del Cosmos, Facultad de Ciencias, 18071 Granada, Spain
[94] Warsaw University Observatory, Aleje Ujazdowskie 4, 00-478 Warszawa, Poland